Received: 7 September 2020 | Revised: 15 November 2020 | Accepted: 19 November 2020
DOI: 10.1111/iar.12375

RESEARCH ARTICLE

Island Arc WILEY

The age and geochemistry of the Bardkish syenite, northwest Iran: Syenite formation during Neo-Tethyan subduction

Amin Jafari[1] | Mohsen Moayyed[1] | Ian S. Williams[2]

[1]Department of Geology, Faculty of Natural Sciences, University of Tabriz, Tabriz, Iran

[2]Research School of Earth Sciences, Australian National University, Canberra, Australian Capital Territory, Australia

Correspondence
Mohsen Moayyed, Department of Geology, Faculty of Natural Sciences, University of Tabriz, Tabriz, Iran.
Email: moayyed@tabrizu.ac.ir

Abstract

SHRIMP U–Pb dating of zircon from two representative samples of the Bardkish syenitic pluton, Urumieh plutonic complex, northwestern Iran, yielded a Late Cretaceous weighted mean $^{206}Pb/^{238}U$ age of 91.1 ±0.8 Ma (Turonian). The pluton is characterized by high K_2O content, Ti–Nb–Ta depletion, enrichment in light rare earth elements and large ion lithophile elements compared to high field strength element, Mg-rich biotite and calcic amphibole, suggesting a shoshonitic affinity. Geochemical features of the Bardkish syenite are consistent with derivation by fractional crystallization of initial mafic parent magmas. It is most likely that primary magma of the syenite originated from a metasomatized subcontinental lithospheric mantle source with minor crustal component, and underwent a fractional crystallization process during its emplacement. The estimates of trapping pressures and temperatures suggest that crystallization began at the middle crustal level (less than 11 km) near 700–730 °C. The generation of the Bardkish syenite could be related to the subduction of Neo-Tethyan oceanic crust beneath the Central Iranian microcontinent and it possibly marks a major magmatic episode prior to the final closure of the Neo-Tethyan ocean in northwest Iran.

KEYWORDS

Iran, Neo-Tethys, Sanandaj-Sirjan zone, SHRIMP zircon U–Pb dating, subduction, syenite

1 | INTRODUCTION

Triassic to Late Miocene subduction of Neo-Tethyan crust beneath the Iranian plate generated numerous granitoid intrusions within the Sanandaj-Sirjan zone (SSZ) (Figure 1). The intrusions, which range in size from small single plutons (< 1 km^2) up to large composite batholiths (> 100 km^2), have geochemical characteristics indicative of derivation from a variety of source materials (igneous and sedimentary) in a variety of tectonic settings (syn-collisional, post-collisional, and syn-orogenic). Most intrusions, however, are calc-alkaline I-type granitoids with features characteristic of emplacement in a continental arc setting (e.g. Berberian & King, 1981; Masoudi, Yardley, & Cliff, 2002; Sepahi & Athari, 2006). Syenitic rocks are a minor component of the igneous suite. Most of these are located in the northwest of the SSZ, in places such as Urumieh (Jafari, Fazlnia, & Jamei, 2018), Piranshahr (Mazhari et al., 2009), Sardasht (Fazlnia, 2018), Saqqez (Sepahi & Athari, 2006), Almogholagh (Amiri et al., 2017; Jamshidi-Badr, Collins, Salomao, & Costa, 2018), Golpaygan (Davoudian, Hamedani, Shabanian, & Mackizadeh, 2007), and Dehgolan (Sarjoughian, Kananian, Haschke, & Ahmadian, 2015). Most of them have been assumed to have formed mainly in an extensional tectonic setting because of their A-type nature and or occurring in association with A-type granitoids (Amiri et al., 2017; Davoudian et al., 2007; Mazhari et al., 2009; Sarjoughian et al., 2015; Sepahi & Athari, 2006).

Although syenites are much less common globally than granites and other plutonic rock types, they occur in great variety and have been extensively studied. Numerous models have been proposed to account for the generation of syenite magma, including (i) partial melting of silicic continental crust (e.g. Tchameni, Mezger, Nsifa, & Pouclet, 2001; Wang, Liu, Wang, & Yan, 2017; Whalen, Currie, &

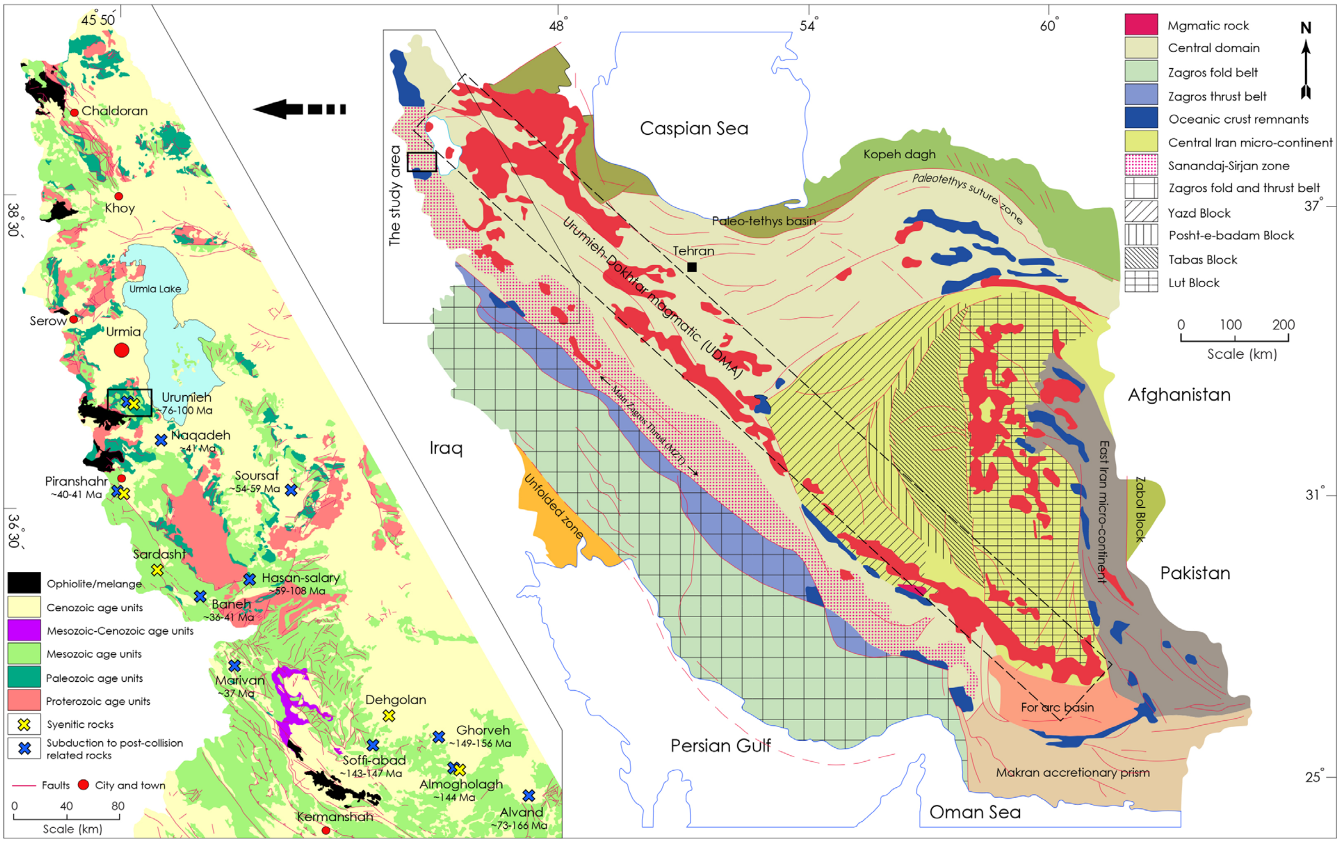

FIGURE 1 Major geological subdivisions of Iran after Stöcklin (1968) and Nabavi (1976), with the location of the study area. Simplified geological map of northwest Iran (on the left hand) compiled using 1:5 000 000 maps of the geological survey of Iran showing subduction to post collision-related intrusive rocks distributions from the northwest SSZ. Further information on these units is presented in Table 6

Chappel, 1987) at pressures typical of the base of over-thickened crust or upper lithospheric mantle (≥ 15 kbar) (Huang & Wyllie, 1981; Wu, Zhang, Gu, Tang, & Lei, 2010); (ii) partial melting of crustal material enriched in large ion lithophile elements (LILEs) by an influx of volatiles (Allen & Chappell, 1992; Lubala, Frick, Roders, & Walraven, 1994); (iii) partial melting of metasomatized mantle rocks (e.g. Lynch, Musselman, Gutmann, & Patchett, 1993; Sutcliffe, Smith, Doherty, & Barnett, 1990); (iv) partial melting of the residue formed by differentiation of K-rich basaltic–andesitic magmas (e.g. Bonin, 2007; Brown & Becker, 1986; Shellnutt, Zhou, & Zellmer, 2009; Thorpe & Tindle, 1992); (v) partial melting of alkali-rich mafic rocks, meta-gabbro, and meta-monzonite (e.g. Eyal, Litvinovsky, Jahn, Zanvilevich, & Katzir, 2010; Jahn, Litvinovsky, Zanvilevich, & Reichow, 2009; Litvinovsky, Jahn, & Eyal, 2015); (vi) mixing of basaltic magma with crustal melt (e.g. Burmakina & Tsygankov, 2013; Mingram, Trumbull, Littman, & Gerstenberger, 2000; Vernikovsky et al., 2003); and (vii) fractional crystallization (with or without crustal assimilation) of mantle-derived magmas (e.g. Litvinovsky et al., 2002; Mingram et al., 2000; Riishuus et al., 2005; Zhu et al., 2017). The petrogenesis of syenite remains a subject of considerable controversy, and some models are in direct conflict with the results of experimental studies. One implication of these different genetic models is that syenite magmas can be emplaced in a variety of tectonic environments within an orogenic cycle (Adetunji, Olarewaju, Ocan, Macheva, & Ganevc, 2018). It is generally assumed, however, that most syenitic magmatism is characteristic of post-orogenic, within-plate, extensional environments (Kaul & Cordiani, 2000; Martin & Devito, 2005; Yang et al., 2005), although several lines of evidence indicate that syenites also can be generated in a syn-orogenic environment during subduction (Chen et al., 2003; Yan & Jiang, 2019).

Here we present the results of a study of the age and geochemistry of the Bardkish syenite, northwest Iran, and discuss their implications for magma petrogenesis and the evolution of an orogenic subduction system associated with the late Cretaceous closure of Neo-Tethys.

2 | GEOLOGICAL SETTING AND FIELD RELATIONSHIPS

The Iranian Plateau is located within the convergence zone between two large, rigid continental plates; the Arabian and Eurasian plates (Hempton, 1987). It is a complex terrane characterized by a diversity of tectonic domains, including continental and oceanic collision zones, each with a different geological style and history (Figure 1). One of the best known tectonic units is the seismically active continent–continent convergent plate boundary in the Zagros Mountains that marks the collision between the Arabian Plate and the central Iranian Plate following subduction of Neo-Tethyan oceanic crust beneath Eurasia (Mohammadi, Rezapour, Sodoudi, & Sadidkhouy, 2014).

The Zagros Orogen, part of the Alpine–Himalayan mountain ranges, consists of several parallel tectonic zones, the main ones being the Urumieh-Dokhtar magmatic arc (UDMA), the SSZ and the Zagros fold and thrust belt (ZFTB) (Figure 1) (Alavi, 1994; Berberian & King, 1981). The UDMA is an Andean-type arc, a belt of intrusive and extrusive rocks about 50 km wide and up to 4 km thick (Berberian & King, 1981), the southeastern section of which is associated with currently active subduction of Indian Ocean crust (McCall, 2002). Calc-alkaline magmatism has continued from the Eocene to the present (e.g. Berberian & King, 1981). The SSZ extends for 1500 km, with an average width of 150 km, from southeastern Iran to northeastern Iraq, and joins the Taurus belt in Turkey (Robertson et al., 2007). It is separated from the ZFTB by the Main Zagros Thrust (MZT) in the southwest, and is bordered by the UDMA in the northeast. It consists mostly of complexly deformed and metamorphosed Mesozoic basement intruded by numerous deformed and un-deformed Mesozoic plutons and widespread Mesozoic volcanic rocks (Mohajjel, Fergusson, & Sahandi, 2003; Sepahi, Ghoreishvandi, Maanijou, Maruoka, & Vahidpour, 2020). The ZFTB, a 150–250 km wide zone between the MZT to the northeast and the Mountain Front Fault to the southwest, consists of thick (13–14 km) folded shelf deposits of late Paleozoic to early Cenozoic age (James & Wynd, 1965). The MZT is interpreted to be the suture zone of the Neo-Tethys Ocean (Sherkati, Letouzey, & Frizon de Lamotte, 2006). Late Cretaceous obduction of ophiolite in the ZFTB marked the start of compressive deformation. Subsequent folding and thrusting were related to the ongoing collision between the Arabian plate and central Iran, starting along the MZT in the in the Late Cretaceous–Early Tertiary (e.g. Sepahi et al., 2020).

The focus of the present study is an area 50 km south of Urumieh, northwest of the SSZ, between the UDMA and ZFTB (Figure 1). There the Bardkish syenite, a single stock within the Urumieh plutonic complex, is intruded into a mafic unit (Gabbro, diorite, and monzodiorite) of late Cretaceous age (Figure 2). Although the dioritic unit, the largest body in the Urumieh complex, is devoid of magmatic enclaves and xenoliths, the more felsic syenite shows evidence of magmatic interaction (mafic microgranular enclaves, and magma mixing and mingling features), indicating that the syenite and mafic magmas were coeval (Figure 3). Permian to Jurassic sedimentary rocks (mainly limestones and shales) are basement to the plutons, which in turn are partly overlain by Early Miocene formations. Numerous faults of probable Cenozoic age cut the plutonic rocks. The dominant structural trend, (faults, folds, and mountains) is northwest–southeast, consistent with the orientation of the SSZ. Mélange consisting of serpentinized pyroxenite, mafic volcanic rocks, radiolarite, and pelagic limestone of Late Cretaceous to Eocene age is the remains of the Neo-Tethyan oceanic lithosphere (Naghizadeh & Ghalamghash, 2005).

3 | ANALYTICAL METHODS

3.1 | Electron probe microanalysis

Electron microprobe analyses of alkali-feldspar, plagioclase, biotite, and amphibole in the syenitic rocks were performed using a Cameca SX100 electron microprobe at Iran Mineral Process and Research Center. Analytical conditions were 15 kV accelerating potential, 20 mA beam current and electron beam diameter of 3 μm. Instrumental calibration was made using natural and synthetic minerals as standards. The detection limit for oxide species was 100 ppm. Representative mineral analyses are presented in Table 1.

3.2 | Major and trace elements

Twenty-two rock samples were collected from syenite unit. After precise microscopic studies, eight fresh rock samples were selected for geochemistry studies. These were chipped using a manual splitter and powdered in a tungsten-carbide ring mill to a grain size of < 200 μm. Aliquots of four powder samples (AJ-3, AJ-4, AJ-9, and AJ-10) were sent to the Australian Laboratory Services (ALS) Brisbane Laboratory, Australia, and four other powder samples (CJ-45, CJ-46, CJ-47, CJ-48) were dispatched to the Arginine Catabolic Mobile Element (ACME) Vancouver Laboratory, Canada, for whole rock analysis. ALS determined the major element oxide concentrations using inductively coupled plasma–atomic emission spectrometry following the lithium borate fusion method (detection limit of 0.01 %, except for Cr_2O_3 with detection limit of 0.002 %) and trace element concentrations using inductively coupled plasma–mass spectrometry (ICP–MS-detection limit 10–0.01 ppm). ACME determined the major and trace element compositions using ICP–MS with, similar detection limit (Table 2).

3.3 | SHRIMP zircon U–Pb dating

3.3.1 | Mineral separation

Zircon was separated from two of the samples (AJ-3 and AJ-9) for U–Th–Pb dating by sensitive high resolution ion microprobe-reverse geometry (SHRIMP RG) at the Research School of Earth Sciences (RSES), Australian National University (ANU). The dust fraction was removed from the crushed whole-rock powder by flushing with water, then the remaining sand dried and density separated in tetrabromoethane (2.96 g/cc) and methylene iodide (3.3 g/cc). A zircon concentrate was then prepared using a Frantz barrier magnetic separator. Zircons were then hand-picked from the final focusing on grains of high clarity as free as possible of discoloration, fractures and inclusions. About 300 grains from each sample were mounted in epoxy resin along with zircon standards (SL13: U = 238 ppm, Williams, 1998; TEMORA2: $^{206}Pb/^{238}U$ = 0.06683, 417 Ma, Black et al., 2004), after which the mount was polished progressively with

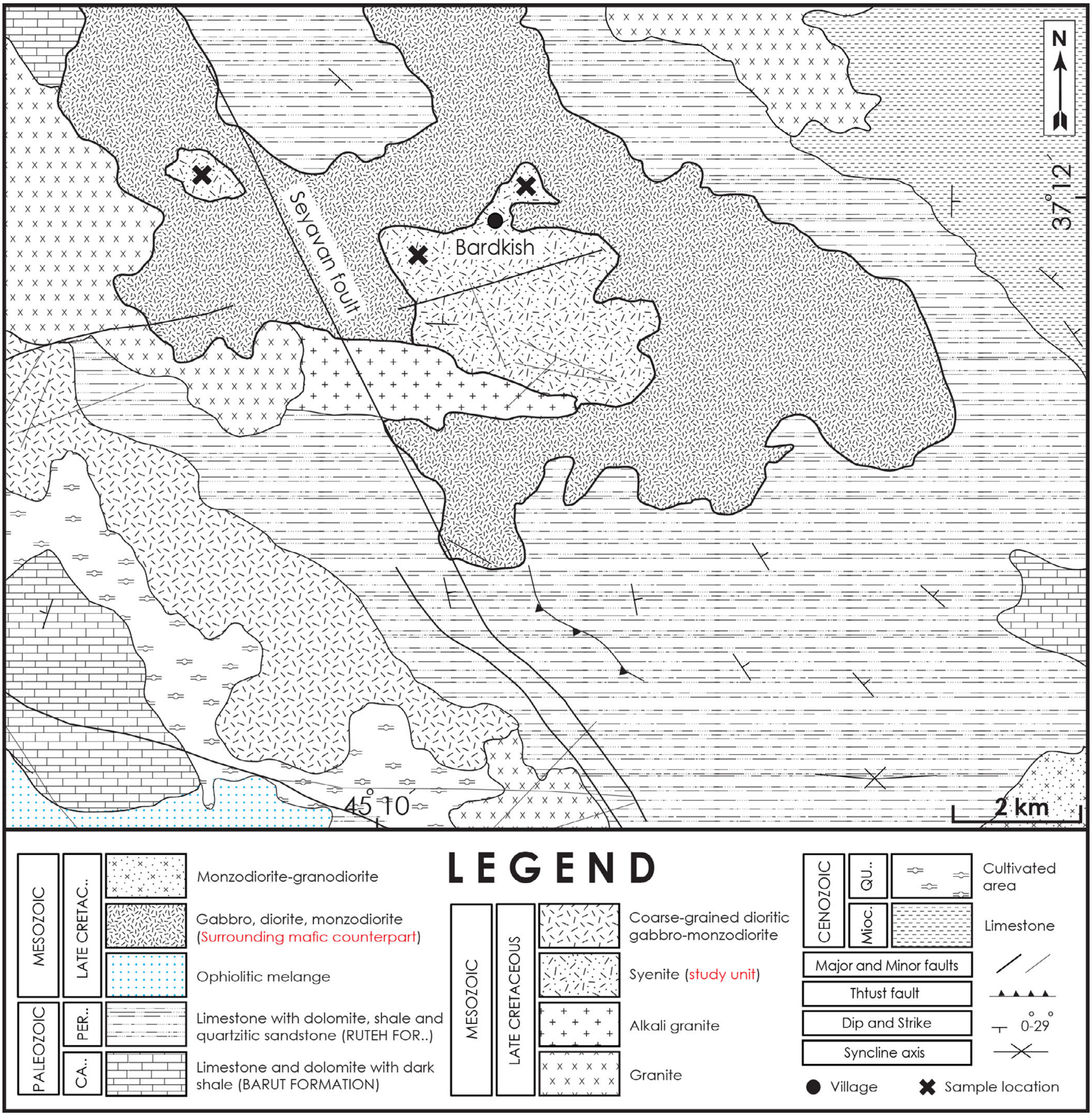

FIGURE 2 Sketch geological map of the study area

1200 grade SiC paper, and 3 and 1 μm diamond emulsion to section the crystals approximately to their centers.

3.3.2 | Imaging

After washing in petroleum spirit, RBS35 detergent solution and Milli-Q ultrapure water the zircon mount was dried for several hours in a 60 °C vacuum oven, then coated by evaporation with 2 nm of high purity Au in preparation for cathodoluminescence (CL) imaging using a Jeol JSM-6610A SEM at the RSES, ANU. Those images revealed the morphology, internal textures and likely paragenesis of the grains. The CL images were then combined with reflected and transmitted light photomicrographs help to identify areas within the zircon grains that were unambiguously igneous and free of imperfections.

3.3.3 | SHRIMP U–Th–Pb isotopic analysis

After imaging the washing procedure was repeated and a thicker (15 nm) Au coating applied before the sample mount was placed

FIGURE 3 A field photograph displaying interaction between mafic and syenite magmas

under high vacuum in SHRIMP RG overnight in preparation for isotopic analysis. The analytical procedures for zircon dating followed methods described by Williams (1998). The isotope ratios and calculated ages were corrected for common Pb using the measured ^{207}Pb and a model common Pb composition consistent with the age of the grain (Cumming & Richards, 1975) using Prawn and Lead software written by Trevor Ireland. All individual dates and weighted mean ages were calculated from the radiogenic $^{206}Pb/^{238}U$. The data were plotted (prior to correction for common Pb) using Isoplot 3 (Ludwig, 2003). For all analyses the uncertainty in the determination of Pb/U and Pb/Th was set to a minimum of 0.5 % to prevent the high precision analyses of high-U spots skewing the calculation of the weighted mean ages. The results are summarized in Tables 3 and 4.

4 | PETROGRAPHY AND MINERAL COMPOSITIONS

The Bardkish syenite is a pale-colored, fine to medium-grained rock with a hypidiomorphic granular texture. It is composed mainly of potassium feldspars (60–65 %), plagioclase (20–25 %), biotite (5–10 %), amphibole (10–15 %), and quartz (< 5 %). Accessory minerals include apatite, titanite, zircon, and magnetite. Sericite (< 4 %), chlorite (< 2 %), and epidote (< 0.5 %) are secondary phases. K-feldspars in different sizes occur as anhedral to subhedral crystals and display Carlsbad twinning, perthitic texture, and dissolved margins (Figure 4a). They show a uniform orthoclase-rich composition with $Or_{87–91}$, $Ab_{8–12}$ and negligible amounts of An (Table 1). Plagioclase crystals are subhedral to euhedral and have oscillatory chemical zoning and in some cases resorbed margins. They are mostly transformed to sericite, partly also to epidote from the center (Figure 4b). Plagioclases are mainly oligoclase with a composition of $Ab_{67–77}$ and An_{18-29}. Amphibole crystals with $Fe_t/(Fe_t + Mg)$ ratio of 0.36 to 0.41 occur mostly as subhedral prisms and are often partly altered to chlorite, biotite and opaque minerals (Figure 4c). They have high CaO contents (10.11–11.44 wt%; Table 1) with Ca_B > 1.5, and are therefore classified as calcic amphibole with a magnesio-hornblende composition (Leake et al., 1997). Minor biotites occur as anhedral to euhedral crystals and have a tabular to bladed appearance and are commonly altered to chlorite (Figure 4d). Biotites are characterized by low MgO (9–10 wt%) and high FeO_{tot} (21–23 wt%) contents with $Mg/(Mg + Fe_t)$ ratios (0.43–0.46) (Table 1). Biotites generally do not show chemical zoning and are classified as Mg-rich biotite and annite with Al and Fe/(Fe + Mg) ratios of 2.26–2.34 and 0.54–0.57 respectively based on the classification of Deer, Howie, and Zussman (1992). Quartz occurs as both medium-grained subhedral and fine-grained crystals enclosed within other minerals.

5 | RESULTS

5.1 | Whole-rock geochemistry

All samples except one (sample AJ-4) plot in the syenite domain on the total alkali-silica classification diagram (Figure 5a). According to data listed in Table 2, they are characterized by a limited range of SiO_2 content (60.7–67 wt%), high contents of Al_2O_3 (16.05–18.7 wt %) and $Na_2O + K_2O$ (9.73–11.52 wt%), moderate contents of total Fe_2O_3 (3.06–5.52 wt%), and low contents of MnO (0.04–0.14 wt%), TiO_2 (0.55–1.07 wt%), P_2O_5 (0.15–0.31 wt%), MgO (0.72–1.44 wt%), and CaO (2.05–3.47 wt%). They all fall in the metaluminous, field on the A/CNK *vs* A/NK diagram (Figure 5b) and in the shoshonite field on plot of Ce/Yb *vs* Ta/Yb (Figure 5c). All samples lie also in the field of I and S-type rocks (Figure 5d) although low A/CNK (0.89–0.98), and the lack of typical peraluminous minerals (e.g. cordierite, andalusite, and garnet) or alkaline mafic minerals (e.g. arfvedsonite, riebeckite, and aegirine-augite), demonstrate that they are not S-type rocks. On the contrary, syenitic rocks from the northwest SSZ (Figure 1) mostly plot in the A-type granitoid field (Figure 5d). Data listed in Table 2 show that all samples have moderate total rare earth element contents (191–293 ppm) and very similar primitive mantle-normalized REE patterns (Figure 6a). There is moderate fractionation and relative enrichment of the light rare earth element (LREE) (La_N/Yb_N = 16–37) and the heavy rare earth elements (HREEs) pattern is relatively flat (Gd_N/Yb_N = 1.5–1.9) (Figure 6a). The Eu anomalies are negligible to slightly positive (Eu/Eu* = 0.92–1.45, average 1.18). The patterns of incompatible elements on the multi-element variation diagram highlight the enrichment in the most LIL elements (e.g. Rb, Ba, Th, La, and U) and LREE with respect to high field strength elements (e.g. Nb, Ta, Ti and P) (Figure 6b), consistent with an arc-related setting. Surrounding mafic rocks (Figure 2) along with intermediate components (Figure 5a) exhibit the same behavior of the elements. All units are generally enriched in LILE and LREE relative to high field strength element and HREE (Supplementary file and Figure 6). However, despite the overall facts, they exhibit some difference in trace element concentrations. REE patterns of the three units are not exactly parallel and the concentrations of MREE and HREE in the syenite rocks are lower than those of the mafic and intermediate rocks

TABLE 1 EPMA analyses of potassium feldspar, plagioclase, amphibole and biotite form the Bardkish pluton (values in wt%)

Mineral	Alkali feldspar			Plagioclase					Biotite			Amphibole				
Spot	Sy-Afd1	Sy-Afd2	Sy-Afd3	Sy-Pl1	Sy-Pl2	Sy-Pl3	Sy-Pl4	Sy-Pl5	Sy-Bt1	Sy-Bt2	Sy-Bt3	Sy-Am1	Sy-Am2	Sy-Am3	Sy-Am4	Sy-Am5
SiO_2	65.87	64.14	65.6	61.03	61.38	62.82	64.17	65.31	35.6	36.95	35.86	45.36	45.12	45.03	46.28	46.34
TiO_2	0	0.02	0.04	0.03	0.03	0.02	0.01	0.01	4.2	4.03	3.89	1.36	1.39	1.46	1.45	1.32
Al_2O_3	19.79	19.99	19.53	23.75	22.84	22.63	22.75	22.49	12.36	12.44	12.78	7.04	6.95	7.11	6.97	6.7
Cr_2O_3	0	0	0	0	0	0	0	0.01	0	0	0.02	0	0	0	0.01	0
V_2O_3	0	0	0	0.01	0	0	0	0.04	0.21	0.24	0.22	0.1	0.09	0.08	0.11	0.1
FeO_t	0.15	0.15	0.19	0.17	0.3	0.26	0.23	0.2	22.94	21.75	22.17	19.34	19.48	19.01	19.3	19.8
MnO	0	0	0	0	0	0.02	0.02	0.01	0.49	0.46	0.49	1	0.98	0.97	1	0.99
MgO	0	0	0	0	0	0	0	0	9.6	10.04	10.46	10.72	10.44	10.66	10.44	10.6
CaO	0.03	0.11	0.05	5.78	4.25	4.78	3.6	3.92	0	0.01	0	11.44	10.97	11.39	10.21	10.11
Na_2O	1.23	0.86	0.77	7.48	9.52	7.55	8.16	7.81	0.14	0.15	0.13	1.69	1.74	1.69	1.75	1.62
K_2O	13	15.58	12.92	0.5	0.6	0.54	0.58	0.19	10.59	10.72	10.52	0.9	0.9	0.94	0.88	0.86
Total	100.07	100.85	99.1	98.75	98.92	98.62	99.52	99.99	96.13	96.79	96.54	98.95	98.06	98.34	98.4	98.44
Structural formula (number of ions) on the basis of 8 oxygens for feldspars, 22 oxygens for biotite and 23 oxygens for amphibole																
Si	3.041	2.929	3.070	2.761	2.732	2.851	2.875	2.926	5.587	5.705	5.572	6.725	6.739	6.719	6.826	6.813
Ti	0.000	0.001	0.001	0.001	0.001	0.001	0.000	0.000	0.496	0.468	0.455	0.152	0.156	0.164	0.161	0.146
Al	1.077	1.076	1.077	1.266	1.198	1.210	1.201	1.188	2.287	2.264	2.341	1.230	1.223	1.250	1.174	1.161
Cr	0.000	0.000	0.000	0.000	0.000	0.000	0.000	0.000	0.000	0.000	0.002	0.000	0.000	0.000	0.001	0.000
Fe^{3+}	0.000	0.006	0.000	0.000	0.011	0.000	0.000	0.000	0.000	0.000	0.000	0.725	0.800	0.673	0.922	1.114
Fe^{2+}	0.006	0.000	0.007	0.006	0.000	0.010	0.009	0.007	3.011	2.808	2.881	1.672	1.633	1.699	1.459	1.320
Mn	0.000	0.000	0.000	0.000	0.000	0.001	0.001	0.000	0.065	0.060	0.064	0.126	0.124	0.123	0.125	0.123
Mg	0.000	0.000	0.000	0.000	0.000	0.000	0.000	0.000	2.246	2.311	2.423	2.369	2.324	2.371	2.295	2.323
Ca	0.001	0.005	0.003	0.280	0.203	0.232	0.173	0.188	0.000	0.002	0.000	1.817	1.755	1.821	1.613	1.592
Na	0.110	0.076	0.070	0.656	0.821	0.664	0.709	0.678	0.043	0.045	0.039	0.486	0.504	0.489	0.500	0.462
K	0.766	0.908	0.771	0.029	0.034	0.031	0.033	0.011	2.120	2.111	2.085	0.170	0.171	0.179	0.166	0.161
An (mol%)	0.16	0.54	0.29	29.02	19.15	25.04	18.89	21.44								
Ab (mol%)	12.55	7.69	8.28	67.98	77.62	71.58	77.48	77.31								
Or (mol%)	87.28	91.75	91.42	2.98	3.21	3.36	3.62	1.23								
Calculated pressure (kbar) using Al-in-Hbl barometer with a precision of ±0.60 (Schmidt, 1992)																
Sample		Sy-Am1 = 2.84			Sy-Am2 = 2.81			Sy-Am3 = 2.94		Sy-Am4 = 2.58				Sy-Am5 = 2.52		
Calculated temperature (°C) using Pl-Hbl pairs thermometer with a precision of ±40 (Holland & Blundy, 1994)																
Sample pairs		Sy-Pl1-Sy-Am1 = 712.4			Sy-Pl2-Sy-Am2 = 700.4			Sy-Pl3-Sy-Am3 = 710			Sy-Pl4-Sy-Am4 = 727.3			Sy-Pl5-Sy-Am5 = 730.5		

TABLE 2 Representative major (in wt%), trace and rare earth element (in μg/g) analyses of syenite rocks from the Bardkish pluton

Sample	AJ-3	AJ-4	AJ-9	AJ-10	CJ-45	CJ-46	CJ-47	CJ-48	LOD* (prefix AJ)	LOD* (prefix CJ)
SiO_2	63.40	67.00	60.70	62.90	62.07	62.43	61.25	60.99	0.01	0.01
TiO_2	0.70	0.55	1.07	0.67	0.75	0.62	0.75	0.66	0.01	0.01
Al_2O_3	18.55	16.05	18.30	17.90	18.01	17.95	17.82	18.73	0.01	0.01
Fe_2O_3	4.28	3.06	5.52	4.06	4.70	4.24	5.13	4.43	0.01	0.04
MnO	0.10	0.05	0.14	0.09	0.11	0.08	0.09	0.09	0.01	0.01
MgO	0.96	0.72	1.44	0.86	1.04	0.88	1.13	0.92	0.01	0.01
CaO	2.57	2.35	3.47	2.05	2.79	2.43	2.80	2.90	0.01	0.01
Na_2O	5.46	4.13	5.65	4.34	5.17	4.53	4.80	5.40	0.01	0.01
K_2O	4.78	5.55	4.44	7.18	4.56	5.94	5.21	4.58	0.01	0.01
Cr_2O_3	< 0.002	< 0.002	< 0.002	< 0.002	0.030	0.033	0.035	0.030	0.002	0.002
P_2O_5	0.20	0.15	0.31	0.17	0.21	0.18	0.20	0.18	0.01	0.01
SrO	0.03	0.03	0.04	0.04					0.01	
BaO	0.12	0.11	0.11	0.21					0.01	
LOI	0.46	0.34	0.27	0.26	0.30	0.40	0.50	0.80	0.01	0.01
Total	101.61	100.09	101.46	100.73	99.72	99.72	99.69	99.71	0.01	0.01
V	38	56	69	42	41	40	60	39	5	8
W	220	338	132	211	< 0.5	0.7	< 0.5	< 0.5	1	0.5
Cr	< 10	< 10	< 10	< 10					10	
Co					5.0	5.2	6.2	4.6		0.2
Ga	20.3	17.3	20.9	19.2	20.5	17.6	22.7	21.4	0.1	0.5
Rb	113	106.5	107.5	192	109.7	126.5	130.7	89.3	0.2	0.1
Sr	316	335	356	368	354.0	367.8	390.4	367.8	0.1	0.5
Y	18	14.8	25.4	15.3	18.8	10.6	17.3	13.5	0.1	0.1
Zr	475	166	395	358	377.6	362.8	476.0	441.1	2	0.1
Nb	55.3	34.8	69.6	43.4	52.3	28.0	43.2	36.4	0.2	0.1
Cs	1.43	0.84	1.12	2.12	1.2	0.9	0.9	0.7	0.01	0.1
Ba	1080	924	958	1800	1083	1328	1163	1158	0.5	1
Hf	10.9	4.5	9.4	8.2	8.1	8.3	10.2	9.4	0.2	0.1
Sn	2	2	2	2	1	< 1	2	1	1	1
Ta	3.3	3.6	3.8	2.9	2.7	1.5	2.4	2.0	0.1	0.1
Pb					1.8	1.9	1.9	1.7		0.1
Th	13.3	15.4	10.05	9.73	14.5	11.3	15.2	14.1	0.05	0.2
U	2.28	3.16	2.02	1.83	1.9	1.8	2.3	2.2	0.05	0.1
La	68.1	26.8	63.4	53.3	88.5	60.2	88.4	87.4	0.1	0.1
Ce	106.5	50.2	105.5	87.4	135.5	87.7	134.9	130.6	0.1	0.1
Pr	9.78	5.18	10.15	8.12	12.10	7.82	11.70	11.26	0.03	0.02
Nd	30.1	17.4	34.1	25.5	37.6	23.6	34.7	33.9	0.1	0.3
Sm	4.5	3.22	5.76	3.83	4.96	2.88	4.92	4.07	0.03	0.05
Eu	1.55	1.03	1.67	1.38	1.40	1.27	1.52	1.52	0.03	0.02
Gd	3.9	2.77	5.32	3.52	4.12	2.49	3.77	3.30	0.05	0.05
Tb	0.53	0.45	0.8	0.49	0.56	0.33	0.51	0.43	0.01	0.01
Dy	3.3	2.77	4.64	2.83	3.42	1.90	3.28	2.44	0.05	0.05
Ho	0.65	0.54	0.95	0.58	0.64	0.37	0.64	0.44	0.01	0.02
Er	1.92	1.55	2.64	1.76	1.82	1.06	1.72	1.37	0.03	0.03
Tm	0.28	0.27	0.43	0.28	0.30	0.16	0.27	0.22	0.01	0.01
Yb	2.08	1.89	2.7	1.79	1.80	1.19	1.64	1.59	0.03	0.05
Lu	0.35	0.27	0.45	0.32	0.31	0.21	0.31	0.28	0.01	0.01

Note: LOD*, limit of detection; LOI, loss on ignition.

TABLE 3 Ion microprobe U–Pb isotopic analyses of zircon from sample AJ-3

Spot no.	U (ppm)	Th (ppm)	Th/U (ppm)	Pb* (ppm)	^{204}Pb/^{206}Pb	±	^{206}Pb/^{238}Ut	±	^{207}Pb/^{206}Pbt	±	^{208}Pb/^{206}Pb*	±	^{208}Pb/^{232}Th*	±	^{206}Pb/^{238}U*	±	AGE 8/32	±	AGE 6/38	±
AJ3-1.1	369	223	0.60	6	0.00071576	0.0005184	0.01420	0.00022	0.0476	0.0014	0.1939	0.0070	0.00456	0.00018	0.01421	0.00023	91.9	3.7	90.9	1.4
AJ3-2.1	1088	903	0.83	18	0.00015046	0.0001077	0.01450	0.00015	0.0476	0.0011	0.2641	0.0065	0.00462	0.00013	0.01450	0.00015	93.1	2.5	92.8	1.0
AJ3-3.1	865	399	0.46	13	0.00018747	0.0003199	0.01405	0.00018	0.0481	0.0008	0.1467	0.0049	0.00446	0.00016	0.01404	0.00018	89.9	3.3	89.9	1.2
AJ3-4.1	449	329	0.73	7	0.0002259	0.0001938	0.01436	0.00023	0.0483	0.0018	0.2455	0.0072	0.00481	0.00016	0.01435	0.00023	97.1	3.3	91.9	1.5
AJ3-5.1	363	294	0.81	6	0.00014141	0.0002461	0.01430	0.00021	0.0468	0.0013	0.2632	0.0066	0.00465	0.00014	0.01432	0.00021	93.8	2.8	91.7	1.3
AJ3-6.1	341	234	0.69	5	0.00011429	0.0002505	0.01434	0.00021	0.0492	0.0014	0.2256	0.0069	0.00471	0.00016	0.01432	0.00021	94.9	3.2	91.6	1.3
AJ3-7.1	396	223	0.56	6	0.00047806	0.0003454	0.01426	0.00023	0.0479	0.0012	0.1732	0.0071	0.00438	0.00020	0.01426	0.00023	88.4	3.9	91.3	1.4
AJ3-8.1	545	478	0.88	9	0.00024905	0.0001873	0.01429	0.00028	0.0481	0.0020	0.2945	0.0082	0.00480	0.00017	0.01429	0.00028	96.7	3.4	91.4	1.8
AJ3-9.1	414	215	0.52	6	0.00024922	0.0002573	0.01461	0.00019	0.0504	0.0013	0.1664	0.0062	0.00466	0.00019	0.01456	0.00019	94.0	3.7	93.2	1.2
AJ3-10.1	669	470	0.70	10	0.00005638	0.000174	0.01431	0.00022	0.0486	0.0016	0.2191	0.0083	0.00446	0.00018	0.01429	0.00022	89.9	3.7	91.5	1.4
AJ3-11.1	530	403	0.76	8	0.00031067	0.0001848	0.01419	0.00017	0.0491	0.0014	0.2477	0.0060	0.00462	0.00013	0.01417	0.00017	93.1	2.6	90.7	1.1
AJ3-12.1	286	203	0.71	5	0.00073761	0.0003389	0.01436	0.00021	0.0494	0.0014	0.2254	0.0078	0.00455	0.00017	0.01434	0.00021	91.8	3.5	91.8	1.4
AJ3-13.1	241	163	0.67	4	0.00047269	0.0006182	0.01441	0.00021	0.0487	0.0025	0.2302	0.0099	0.00491	0.00023	0.01439	0.00021	99.0	4.5	92.1	1.4
AJ3-14.1	332	215	0.65	5	0.00011501	0.0002938	0.01470	0.00033	0.0482	0.0018	0.2098	0.0102	0.00476	0.00026	0.01469	0.00033	96.0	5.2	94.0	2.1
AJ3-15.1	409	370	0.90	7	0.00002929	0.0002059	0.01376	0.00015	0.0463	0.0017	0.2983	0.0091	0.00455	0.00015	0.01379	0.00016	91.7	3.0	88.3	1.0
AJ3-16.1	926	487	0.53	14	0.00002	0.0001041	0.01416	0.00018	0.0498	0.0014	0.1662	0.0054	0.00447	0.00016	0.01413	0.00018	90.1	3.2	90.4	1.2

Note: "*" indicates the radiogenic portion; detection limit for isotopic ratios are about 2.5 ppb; "t" indicates total value; errors are 1σ (1 sigma); age (Ma).

TABLE 4 Ion microprobe U–Pb isotopic analyses of zircon from sample AJ-9

Spot no.	U (ppm)	Th (ppm)	Th/U (ppm)	Pb* (ppm)	^{204}Pb/^{206}Pb	±	^{206}Pb/^{238}Ut	±	^{207}Pb/^{206}Pbt	±	^{208}Pb/^{206}Pb*	±	^{208}Pb/^{232}Th*	±	^{206}Pb/^{238}U*	±	AGE 8/32	±	AGE 6/38	±
AJ9-1.1	661	631	0.96	10	0.00071576	0.0005184	0.01310	0.00014	0.0479	0.0010	0.2988	0.0061	0.00410	0.00010	0.01310	0.00014	82.7	1.9	83.9	0.9
AJ9-2.1	453	254	0.56	7	0.00015046	0.0001077	0.01405	0.00032	0.0486	0.0016	0.1807	0.0064	0.00452	0.00020	0.01404	0.00032	91.1	4.0	89.9	2.0
AJ9-3.1	1800	1375	0.76	28	0.00018747	0.0003199	0.01389	0.00020	0.0480	0.0009	0.2383	0.0037	0.00433	0.00010	0.01389	0.00020	87.3	2.0	88.9	1.3
AJ9-4.1	322	169	0.52	5	0.0002259	0.0001938	0.01391	0.00025	0.0483	0.0014	0.1764	0.0073	0.00468	0.00021	0.01390	0.00025	94.3	4.3	89.0	1.6
AJ9-5.1	394	316	0.80	6	0.00014141	0.0002461	0.01415	0.00022	0.0514	0.0017	0.2504	0.0082	0.00440	0.00016	0.01408	0.00022	88.6	3.3	90.2	1.4
AJ9-6.1	379	248	0.65	6	0.00011429	0.0002505	0.01402	0.00027	0.0505	0.0020	0.2125	0.0096	0.00454	0.00023	0.01397	0.00027	91.6	4.6	89.5	1.7
AJ9-7.1	596	512	0.86	10	0.00047806	0.0003454	0.01411	0.00017	0.0498	0.0013	0.2662	0.0071	0.00436	0.00013	0.01408	0.00017	87.9	2.6	90.1	1.1
AJ9-8.1	355	259	0.73	6	0.00024905	0.0001873	0.01430	0.00022	0.0496	0.0013	0.2183	0.0064	0.00427	0.00014	0.01426	0.00022	86.2	2.9	91.3	1.4
AJ9-9.1	510	513	1.01	9	0.00024922	0.0002573	0.01447	0.00025	0.0493	0.0013	0.3195	0.0077	0.00459	0.00014	0.01444	0.00025	92.5	2.8	92.4	1.6
AJ9-10.1	601	497	0.83	10	0.00005638	0.000174	0.01424	0.00021	0.0490	0.0013	0.2728	0.0068	0.00469	0.00014	0.01422	0.00021	94.6	2.8	91.0	1.4
AJ9-11.1	486	313	0.64	8	0.00031067	0.0001848	0.01474	0.00014	0.0480	0.0013	0.2066	0.0056	0.00472	0.00014	0.01473	0.00014	95.3	2.7	94.3	0.9
AJ9-12.1	509	262	0.51	8	0.00073761	0.0003389	0.01423	0.00025	0.0491	0.0011	0.1753	0.0059	0.00484	0.00019	0.01421	0.00025	97.6	3.8	90.9	1.6
AJ9-13.1	318	246	0.77	5	0.00047269	0.0006182	0.01435	0.00033	0.0494	0.0014	0.2394	0.0109	0.00444	0.00023	0.01432	0.00033	89.5	4.6	91.7	2.1
AJ9-14.1	447	449	1.00	8	0.00011501	0.0002938	0.01553	0.00017	0.0485	0.0012	0.3291	0.0074	0.00509	0.00013	0.01552	0.00018	102.6	2.6	99.3	1.1
AJ9-15.1	299	168	0.56	5	0.00002929	0.0002059	0.01440	0.00040	0.0495	0.0014	0.1652	0.0068	0.00424	0.00022	0.01437	0.00040	85.5	4.4	92.0	2.6
AJ9-16.1	465	341	0.73	8	0.00002	0.0001041	0.01469	0.00021	0.0505	0.0017	0.2275	0.0067	0.00454	0.00015	0.01464	0.00021	91.6	3.0	93.7	1.3

Note: "*" indicates the radiogenic portion; detection limit for isotopic ratios are about 2.5 ppb; "t" indicates total value; errors are 1σ (1 sigma); age (Ma).

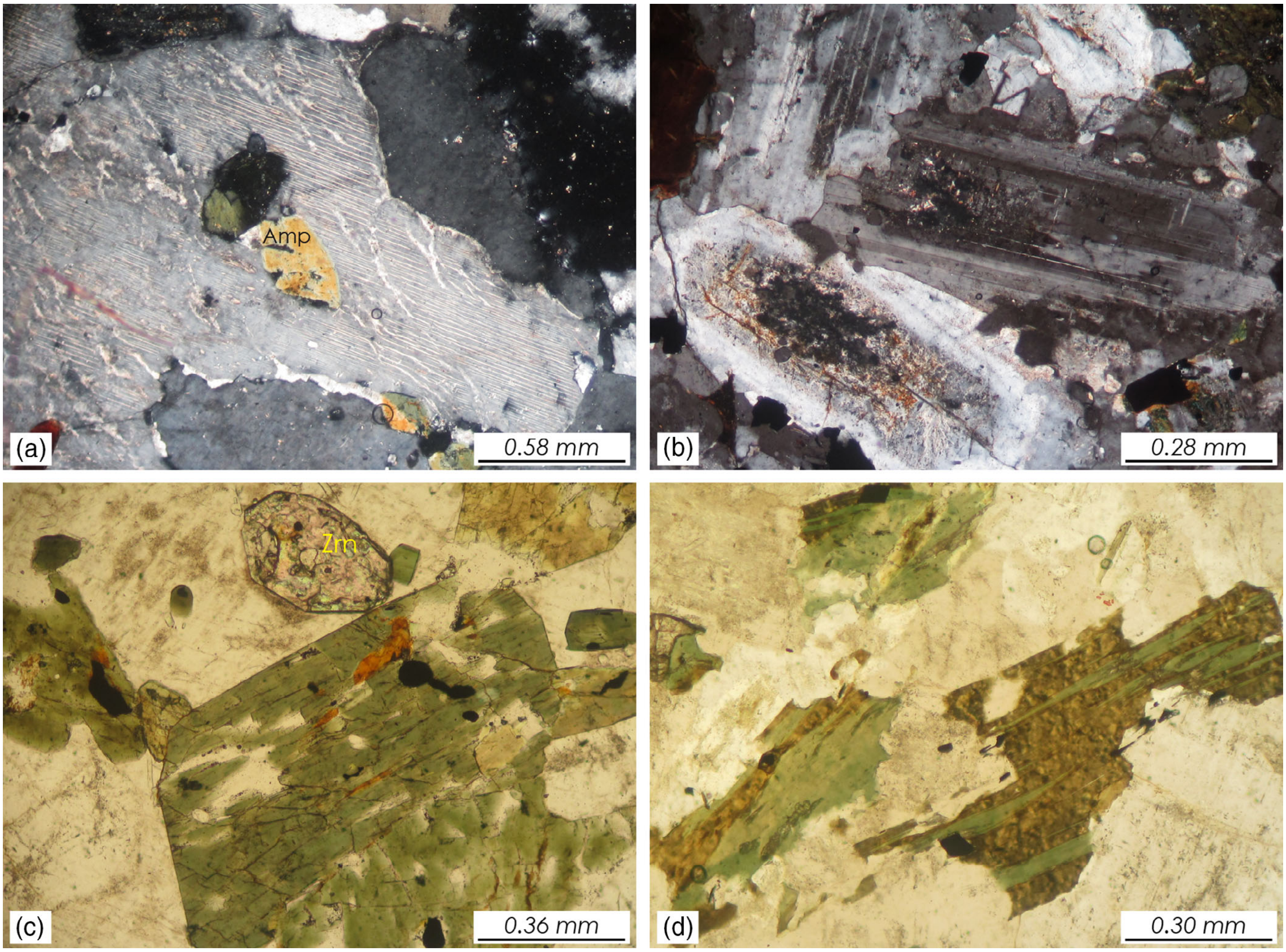

FIGURE 4 Photomicrographs of Bardkish syenite. (a) Perthitic orthoclase phenocryst indicating inclusion of patchy amphibole. (b) Plagioclase crystals with chemical zoning, marginal dissolution and evidence of sericitization in the core. (c) Amphibole crystals in different sizes showing partly alteration to chlorite, biotite and opaque minerals. (d) Alteration of magmatic biotite to chlorite

(Figure 6a). In addition, syenites are enriched in some LILE (e.g. Rb, K and Ba) and depleted in Ti and P (Figure 6b). Fractional crystallization modeling shows that overall depletion in MREEs to HREEs and enrichment of LREEs of the syenites are mainly controlled by garnet fractionation (Figure 7a). In addition, controlling factor for LIL elements in the syenite rocks could be explained by fractionation of both plagioclase and amphibole (Figure 7b).

5.2 | SHRIMP zircon U–Pb dating

SHRIMP U–Pb isotopic analyses of zircon from samples AJ-3 and AJ-9 are listed in Tables 3 and 4 respectively. The zircon grains from these samples are very similar. They are stubby, 100–200 μm in diameter, colorless to pale brown, mostly euhedral to subhedral crystals with a prismatic habit. All zircons have well-developed oscillatory zoning, typical of growth under magmatic conditions (Figures 8a and 9a). In some zircon grains there is a discontinuity zoning between the center (commonly dark in CL) and the outer oscillatory zones, consistent with the presence of an older core. Apatite and melt inclusions are common.

Sixteen crystals from each sample were analyzed isotopically for U–Th–Pb. Most analyses targeted melt-precipitated zircons with oscillatory zoning. One analysis from each sample targeted a dark-CL core. The zircons from sample AJ-3 have low to moderate U (240–-1090 ppm) and Th (160–900 ppm) contents, with Th/U ratio between 0.46 and 0.90. Pb contents are very low (a few ppb), so even without common Pb correction the U–Pb analyses plot on concordia within analytical uncertainty (Figure 8b). Radiogenic $^{206}Pb/^{238}U$ in all spots, even in the dark cores, is the same within analytical uncertainty (MSWD = 1.2), giving a weighted mean age of 91.3 ±1.1 Ma (95 % confidence interval which includes the uncertainty in the analysis of the standard). The zircon grains from sample AJ-9 have a similar range in composition (U 300–660 ppm, Th 170–630 ppm, Th/U 0.51–1.01), except for the cores, in which the U and Th contents are significantly higher (U 1800 ppm, Th 1375 ppm). Most analyses are concordant within analytical uncertainty (Figure 9b), but there is significant scatter in the radiogenic $^{206}Pb/^{238}U$ (MSWD = 9.4). The scatter is due to two

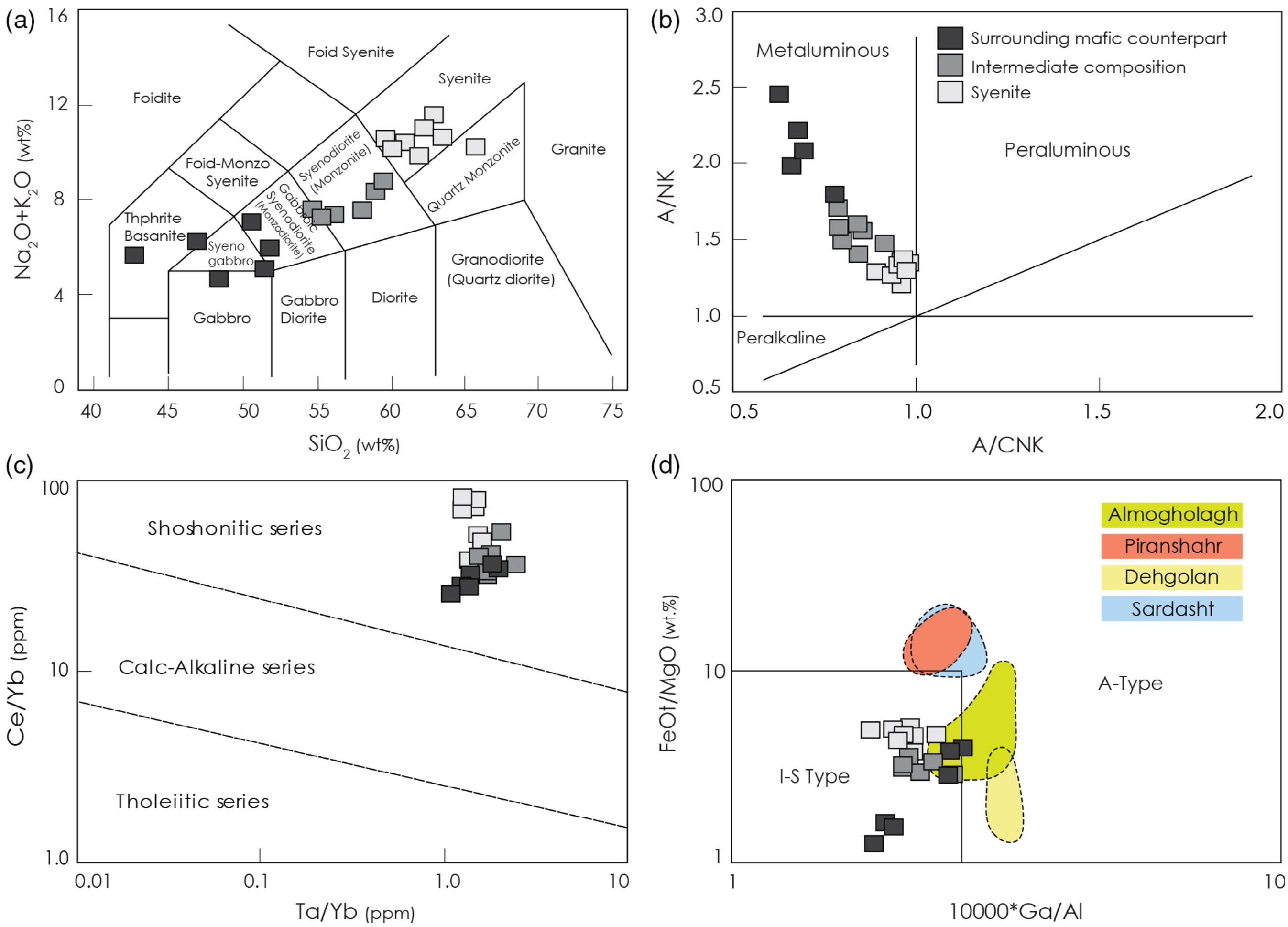

FIGURE 5 (a) Alkali-silica diagram (TAS) for the chemical classification of plutonic rocks (Le Bas, Le Maitre, Streckeisen, & Zanettin, 1986). (b) Peraluminous, metaluminous, and peralkaline discrimination by molar Al_2O_3/CaO + Na_2O + K_2O (A/CNK) *vs* Al_2O_3/Na_2O + K_2O (A/NK) ratios (Maniar & Piccoli, 1989). (c) Diagram of Ce/Yb *vs* Ta/Yb (Pearce, 1983). (d) Diagram of 10 000 * Ga/Al *vs* FeO_t/MgO (Whalen al., 1987), showing the generalized fields of study rocks and other syenitic units from the northwest SSZ. Mafic and intermediate trace-element data is provided in Supplementary file

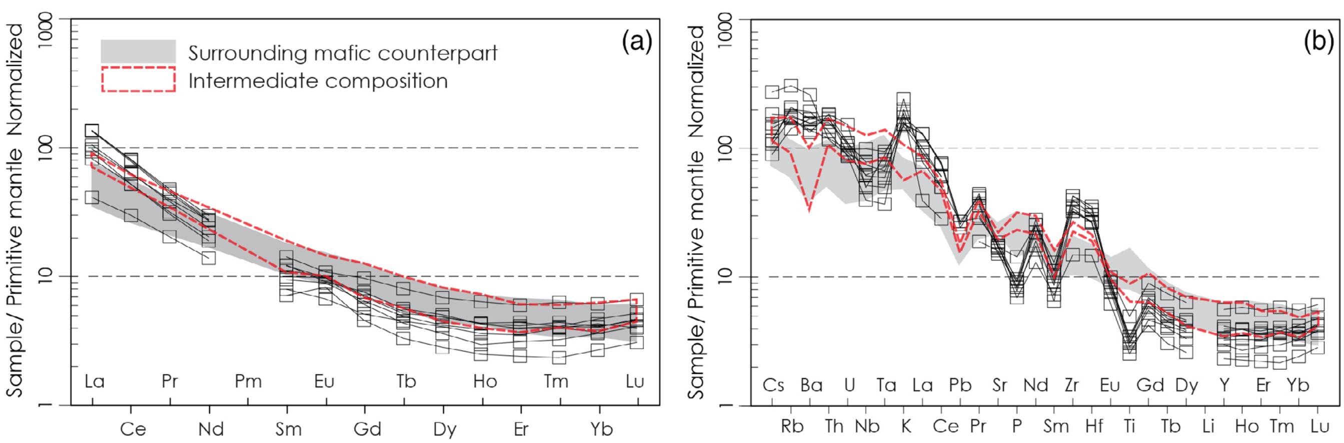

FIGURE 6 (a) Primitive mantle normalized REE compositions and (b) primitive mantle-normalized multi-element patterns for the Bardkish syenite. REE and multi-elements normalizing values are from McDonough and Sun (1995) and Sun and McDonough (1989) respectively. Mafic and intermediate trace-element data are provided in Supplementary file

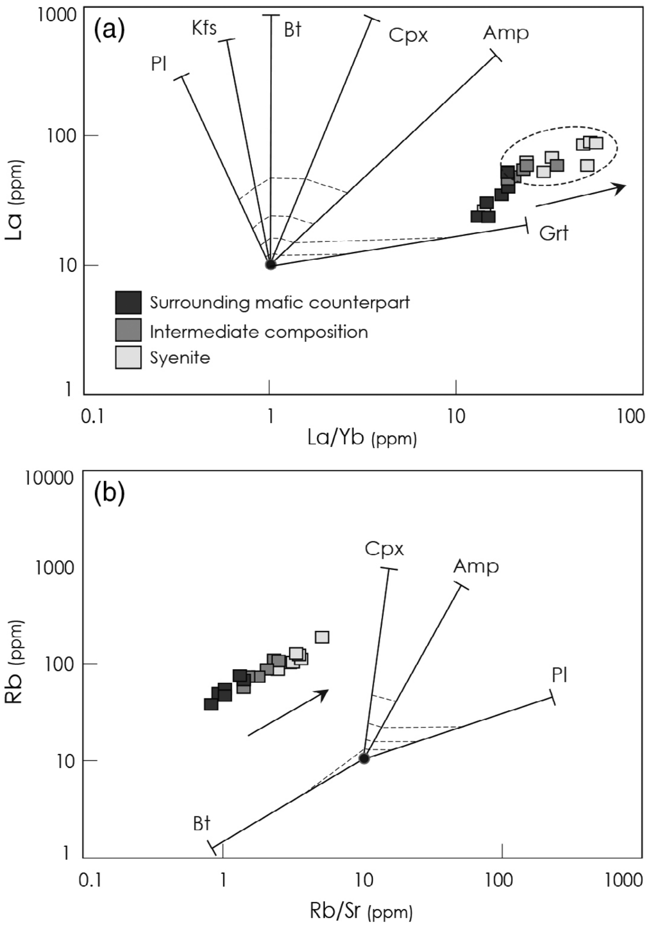

FIGURE 7 (a) La *vs* La/Yb, and (b) Rb *vs* Rb/Sr variation diagrams showing fractional crystallization of main rock-forming minerals of the Bardkish syenite and its counterparts. Partition coefficients based on values of www.earthref.org/KDD. Dotted lines in fractionation trends indicate percentage of mineral assemblage removed, by 20 intervals. Abbreviations for minerals are based on Whitney and Evans (2010); Amp, amphibole; Bt, biotite; Cpx, clinopyroxene; Grt, garnet; Kfs, K-feldspar; Pl, plagioclase

major outliers (one high and one low), and one subtle high outlier (AJ-9-14.1). None of the outliers is the analysis of the single dated core. Omitting the outliers leaves 13 determinations of radiogenic $^{206}Pb/^{238}U$ ratios that are equal within analytical uncertainty, the weighted mean yields an age of 90.7 ±1.3 Ma (MSWD = 0.93). The ages measured on both syenite samples are the same within analytical uncertainty, giving a weighted mean of 91.1 ±0.8 Ma as the best estimate for the intrusion age of the Late Cretaceous Bardkish syenite (Turonian).

6 | DISCUSSION

6.1 | Pressure and temperature (P–T)

As a geobarometer, the Al contents of calcic amphiboles (method of Al-in-hornblende) have been widely used in plutonic rocks (e.g. Anderson & Smith, 1995; Hammarstrom & Zen, 1986; Hollister, Grisson, Peters, Stowell, & Sisson, 1987; Johnson & Rutherford, 1989; Schmidt, 1992). Here, we applied the barometer proposed by Schmidt (1992) to estimate the rock forming pressure/depth of the Bardkish syenite. All samples from the pluton have a mineral assemblage of quartz, plagioclase, hornblende, K-feldspar, biotite, titanite, and magnetite, meeting the prerequisite conditions for the barometer. Calculated pressure results for amphiboles range from 2.52 to 2.94 ±0.60 kbar (Table 1). Using a conversion factor of 10 kbar equal 37 km for continental crust (Tulloch & Challis, 2000), the intrusion depth is estimated to be less than ~ 11 km, indicating that the Bardkish syenite crystallized at intermediate crustal depths. Magma temperatures were calculated using individual hornblende-plagioclase pairs for different samples. Accordingly a crystallization temperature ranging from 700 to 730 ±40 °C at calculated pressure according to Schmidt (1992) was obtained from this geothermometer (Holland & Blundy, 1994) in the syenites (Table 1). Estimated crystallization P–T condition of Bardkish syenite by Al-in-amphibole and hornblende-plagioclase pairs are plotted in Figure 10. As shown, syenite yielded a P–T solution above granite to tonalite solidus, suggestive a uniform P–T condition of the representative amphibole from core to rim.

6.2 | Petrogenesis

Even allowing for the high solubility of zircon in alkaline magmas (Gervasoni, Klemme, Rocha-Júnior, & Berndt, 2016), the lack of inherited zircon in the dated samples suggests that the Bardkish syenite was not generated by the partial melting of ancient basement rocks. The syenite samples have relatively high mg-numbers (29–34) [100 × atomic ratios of Mg/(Mg + Fe)], significantly higher than the mg-number of felsic melts produced experimentally from the partial melting of basalts (Rapp & Watson, 1995). This suggests that they formed from a mafic primary magma and are unlikely to be pure crustal melts.

Mafic, intermediate, and syenite rock types have comparable trace elements behavior (Figure 6) and define parallel independent trends in plots such as Rb *vs* Rb/Sr or Nb *vs* Nb/Yb (Figure 7b,c), thus revealing that the mafic and felsic rocks can be the result of fractionation of a single parental magma. The results of quantitative major and trace elements fractional crystallization model using a least-squares mass balance calculation (Table 5) suggest that it is feasible for the monzonite and syenite to be derived subsequently from the mafic unit by fractional crystallization. The large volume of surrounding mafic rocks provides supporting evidence for the fractional crystallization (Figure 2). Plot of incompatible (Th) *vs* compatible (V) elements (Figure 11a) shows the vector of possible fractional crystallization. Furthermore, the ratios of highly incompatible and moderately incompatible elements (La/Ce) remain unchanged as La increases (Figure 11b), suggesting that the syenite represents the end product of the fractional crystallization from the mafic counterpart. Evidence of magma interactions (Figure 3) favors the coupling of

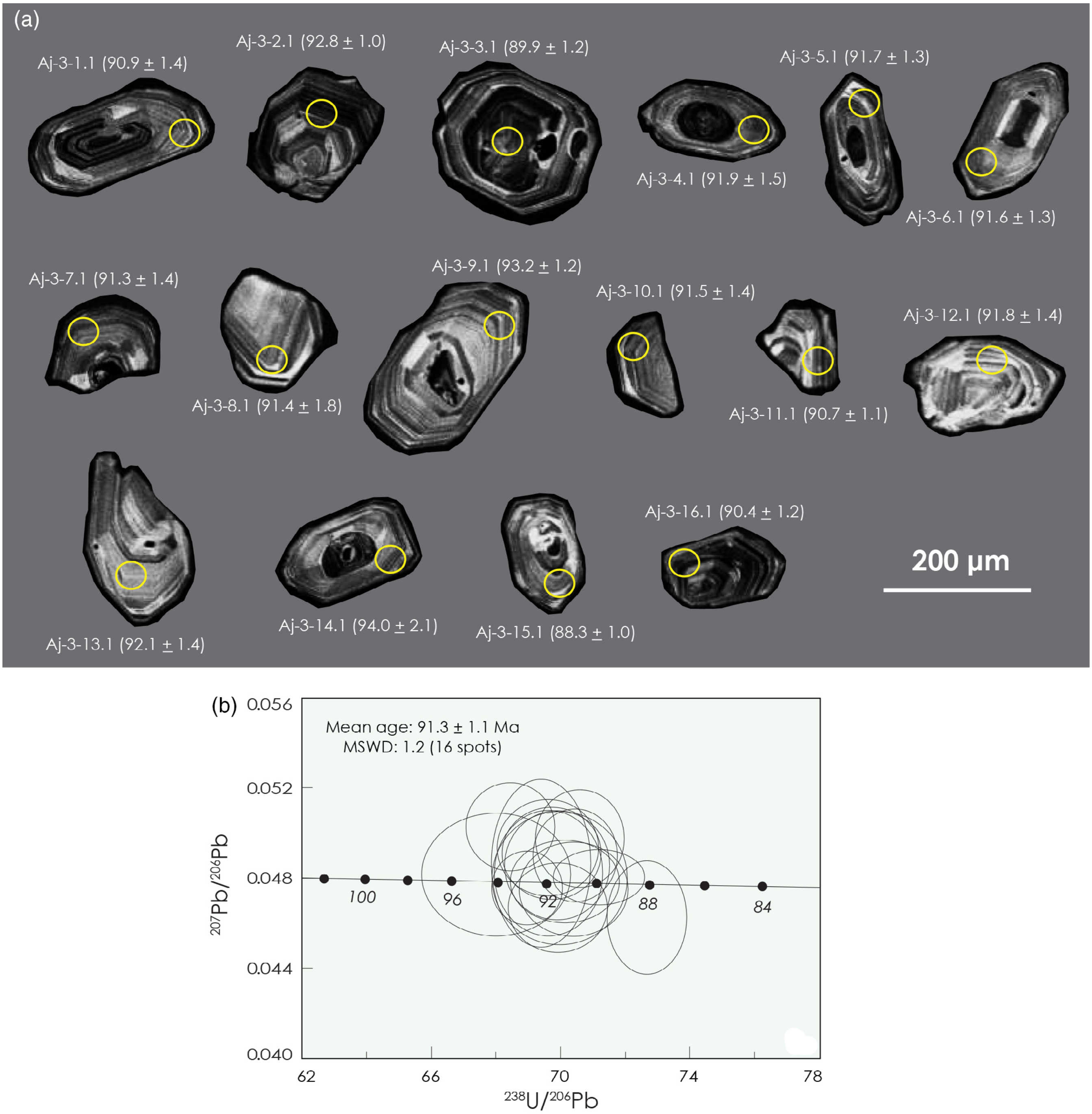

FIGURE 8 (a) Representative zircon cathodoluminescence (CL) images of analyzed spots and (b) U–Pb concordia diagram from sample AJ-3 analyzed by ion microprobe

mixing and fractional crystallization processes leading to simultaneous mixing-fractionation of coeval mafic and felsic magmas (Bora, Kumar, Yi, Kim, & Lee, 2013; Kumar, Pieru, Rino, & Hayasaka, 2017). Positive Zr–Hf and negative Ta–Nb–Ti anomalies (e.g. Swain, Barovich, Hand, Ferris, & Schwarz, 2008; Zhu et al., 2014) in the spider diagram (Figure 6b) and high Th/Ce (0.1–0.3) in the studied samples also indicate that Bardkish syenite has experienced some crustal contamination, since mantle-derived magmas have low Th/Ce ratio (0.02–0.05, Sun & McDonough, 1989).

The samples of Bardkish syenite have geochemical characteristics typical of I-type rocks, most notably high total alkalies (K_2O + Na_2O > 5 wt%), high K_2O/Na_2O, low TiO_2, high and variable Al_2O_3, enrichment in LILEs and LREEs and depletion in Ti–Nb–Ta, all features of shoshonitic series rocks (Morrison, 1980; Turner et al., 1996). Furthermore, Mg-rich biotite and calcic amphibole in the studied syenite are typical of shoshonitic rocks (Jiang et al., 2002; Morrison, 1980), which are distinct from A-type granitoids that generally contain Fe-rich biotite and sodic amphibole

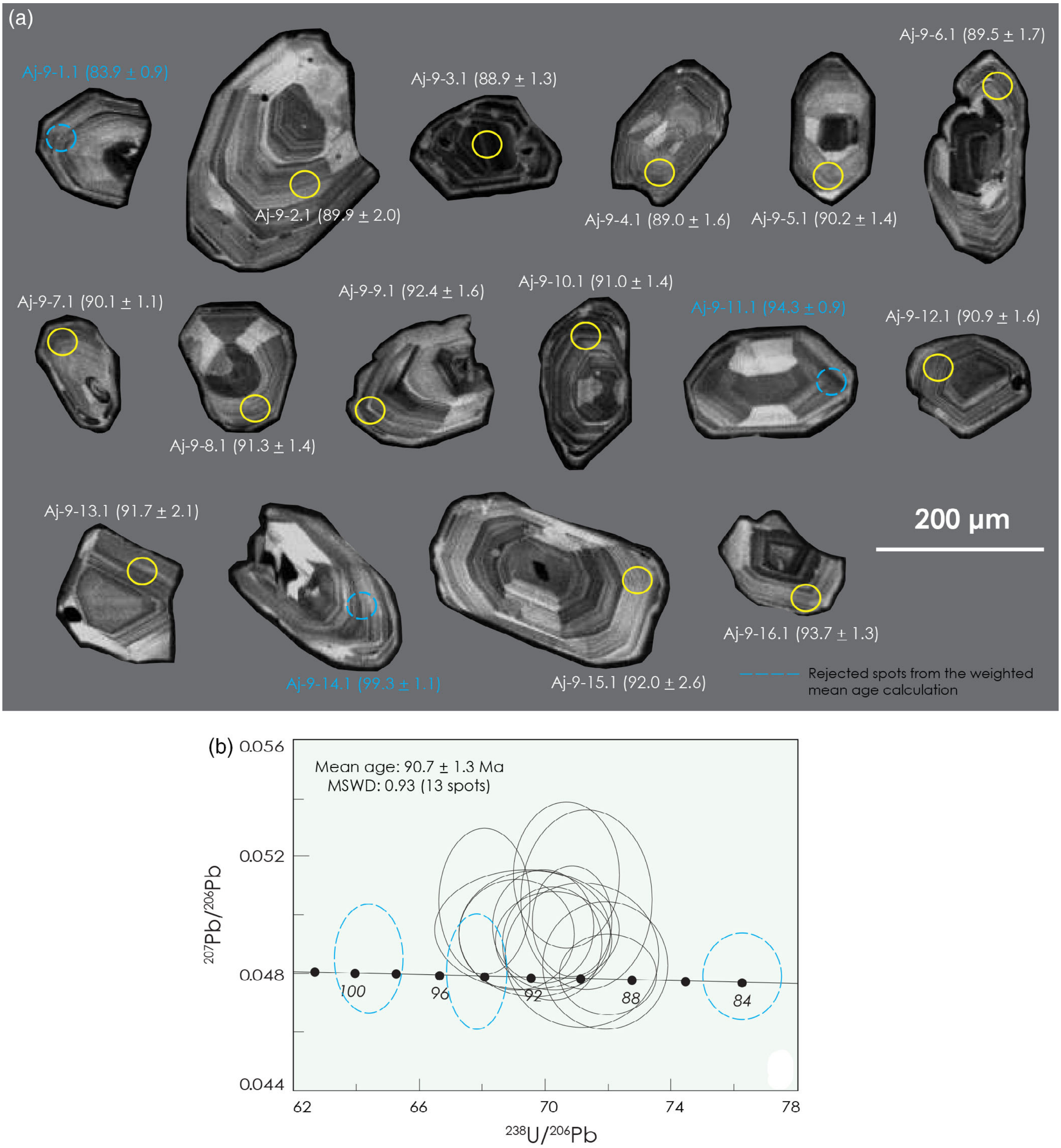

FIGURE 9 (a) Representative zircon cathodoluminescence (CL) images of analyzed spots and (b) U–Pb concordia diagram from sample AJ-9 analyzed by ion microprobe

(Jiang et al., 2002). Shoshonitic rocks are most commonly related to arc settings. They are interpreted as being associated with melts from sub-continental lithospheric mantle sources enriched in incompatible elements by metasomatic and magmatic processes (hydrous fluids and/or melts) in subduction zones (Chen, Chen, & Jahn, 2009; Ferreira et al., 2015; Wang et al., 2017). Bardkish syenite has whole-rock initial $^{87}Sr/^{86}Sr$ ranging from 0.712781 to 0.725305 with εNd values of 3.26 to 3.69 and zircon εHf values of 0.54 to 3.91 (Armon, 2017), providing isotopic evidence for its origination from a sub-continental mantle-derived magma.

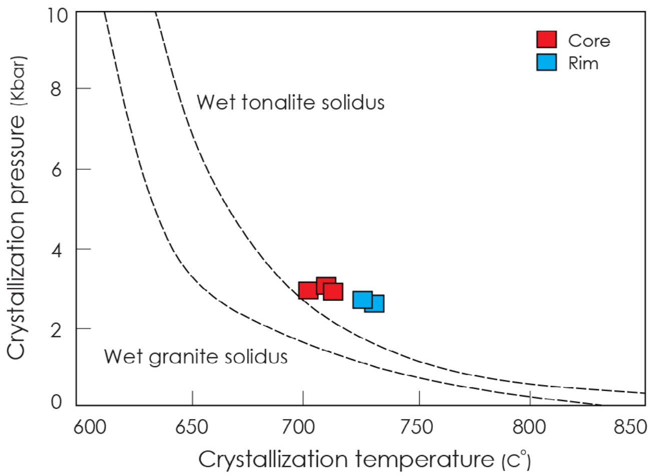

FIGURE 10 Crystallization temperature *vs* pressure diagram (Anderson & Smith, 1995), indicating uniform P–T condition of the representative amphibole from core to rim. Curves of wet granite and tonalite solidus are from Anderson, Barth, Wooden, and Mazdab (2008)

The relatively high La/Nb (1.86–2.58) and the degree of LREE enrichment show that the syenite magma was not generated from either a depleted or primitive mantle source. La/Yb in asthenospheric or primitive mantle commonly ranges from 9 to < 1, but in the syenite samples is 23.5 to 55. Such high La/Yb requires sources enrichment in LREE and LILE. The presence of hydrous minerals such as biotite and hornblende indicates that the lithospheric mantle source of the syenite magma had been metasomatized (Berger, Burri, Alt-Epping, & Engi, 2008; Slagstad, Jamieson, & Culshaw, 2005). In the Ba/La *vs* Th/Yb diagram (Figure 11c) all samples plot along a trend consistent with melt-related subduction metasomatism. Hydrous fluids released from subducted sediments into the sub-continental mantle have played an important role in the source enrichment. The infiltration of slab-derived fluids probably generated partial melts in the lithospheric mantle and subsequent I-type rocks were formed by fractional crystallization. The experimental studies have shown that potassic magma can be formed as a result of the interaction between hydrous fluids (or melt) and mantle peridotite (Wyllie & Sekine, 1982).

TABLE 5 Major element fractional crystallization models for Bardkish syenite

	Stage 1: monzodiorite to monzonite					Stage 2: monzonite to syenite				
wt%	Parent (AJ-19)	Daughter (CJ-43)	Calc. Daughter	Subtracted phases	vol%	Parent (AJ-17)	Daughter (AJ-3)	Calc. Daughter	Subtracted phases	vol%
SiO_2	50.90	55.51	55.29	Plagioclase	18.53	58.20	63.40	63.56	Plagioclase	22.18
TiO_2	2.49	1.73	1.45	Amphibole	10.55	1.85	0.70	0.53	Amphibole	20.73
Al_2O_3	17.40	17.74	18.17	Biotite	20.63	16.90	18.55	18.11	Ilmenite	1.54
FeO*	9.80	7.14	7.79	Titanite	0.56	6.83	3.85	4.01	Titanite	1.63
MnO	0.18	0.18	0.14			0.16	0.10	0.00		
MgO	4.02	2.54	1.78			2.63	0.96	0.31		
CaO	6.54	5.49	5.98	Dght%	49.73	5.52	2.57	2.61	Dght%	53.90
Na_2O	4.41	5.65	5.36	Σr^2	1.78	5.36	5.46	5.62	Σr^2	1.89
K_2O	2.69	1.70	1.32			2.27	4.78	3.70		

Note: Σr^2, sum of the square of the residuals.

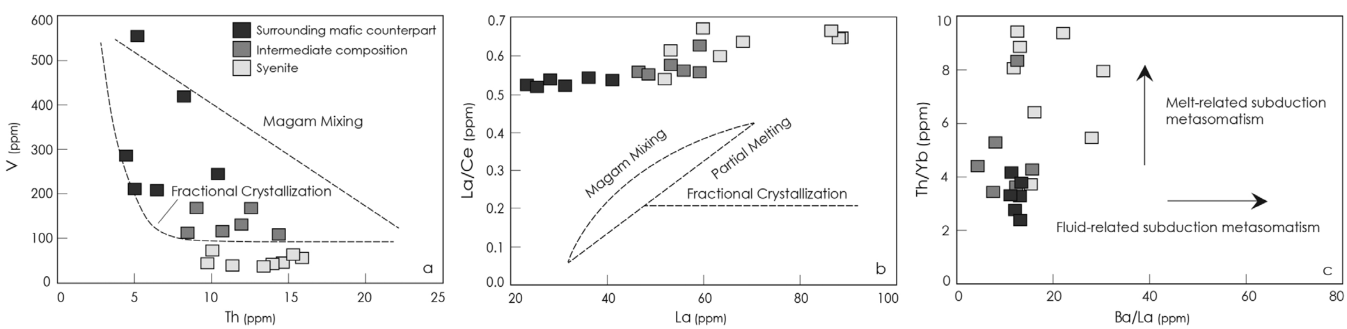

FIGURE 11 (a) Th *vs* V diagram indicating mixing and fractional crystallization trends (Mushkin, Navon, Halicz, Hartmann, & Stein, 2003). (b) Discrimination diagram of La *vs* La/Ce for fractional crystallization, partial melting and magma mixing (Schiano, Monzier, Eissen, Martin, & Koga, 2010). (c) Ba/La *vs* Th/Yb diagram (Woodhead, Hergt, Davidson, & Eggins, 2001). Mafic and intermediate trace-element data is provided in Supplementary file

6.3 | Geodynamic implications

The detachment of Central Iran from Arabia and its northwestward movement led to the formation of the Neo-Tethys Ocean along the present main Zagros fold-thrust belt at the eastern margin of Gondwana. The exact timing of the opening within the period Late Carboniferous to Late Permian is a subject of debate (e.g. Angiolini, Balini, Garzanti, Nicora, & Tintori, 2003; Arefifard, 2017; Sepehr & Cosgrove, 2004; Stampfli, 2000; Zanchi et al., 2009). Nevertheless, the distribution of Mesozoic subduction-related rocks in a narrow northwest–southeast trending band delineated by ophiolitic-mélange belts (Figure 1) indicates that Neo-Tethys subduction was active during the Early to Middle Jurassic (Figure 12) (e.g. Ahadnejad, Valizadeh, Deevsalar, & Rezaei-Kahkhaei, 2011; Arvin, Pan, Dargahi, Malekizadeh, & Babaei, 2007; Chiu et al., 2013; Shahbazi et al., 2010), as evidenced by well-exposed late Triassic I-type plutonic rocks in the southeastern part of the SSZ (Arvin et al., 2007; Hassanzadeh & Wernicke, 2016). Based on isotope geochronological data from major plutonic rocks from northwest part of the SSZ (Table 6) and Neo-Tethyan oceanic lithosphere of Chaldoran (Rezaei Bargoshadi, Moazzen, & Yang, 2019), Khoy (Ghazi, Pessagno, Hassanipak, Duncan, & Babaie, 2003; Khalatbari Jafari, Juteau, & Cotton, 2006), Serow (Rezaii & Moazzen, 2014), Piranshahr (Hajialioghli & Moazzen, 2014), and Kermanshah (Allahyari, Saccani, Pourmoafi, Beccaluva, & Masoudi, 2010) (Figure 1), collision between Arabian margin and north SSZ initiated in the late Cretaceous (Figure 12). Also, the Amiran formation conglomerates of Maastrichtian–Paleocene age have ophiolite clasts, showing that the emplacement time of these ophiolites is pre-Maastrichtian (Ajirlu, Moazzen, & Hajialioghli, 2016). The geochemical and geochronological features of the samples of Bardkish syenite and their position on tectono-magmatic evolution of the Neo-Tethys favor an arc-related magma that formed in an arc setting, possibly recording the closure of Neo-Tethys and the cessation of subduction beneath the Iranian plate, a major late Cretaceous magmatic episode (Figure 12). Hence, syenites in the northwest SSZ are classified into three distinct petrological units in pre-and-after collisional setting (Figures 1 and 11). The youngest unit constitutes the post-collision A-type syenites with Eocene age which have been described in Piranshahr (Mazhari et al., 2009) and Sardasht areas (Fazlnia, 2018). The present zircon U–Pb dating establishes that the Bardkish syenite crystallized in the Turonian (91.1 ±0.8 Ma), forming the subduction-related unit. The oldest unit is late Jurassic to early Cretaceous A-type syenites exposed in areas of Dehgolan (Sarjoughian et al., 2015) and Almogholagh (Amiri et al., 2017; Jamshidi-Badr et al., 2018). Their generation is controversial and is generally inferred to be generated during extensional strain in an intra-arc setting. Such A-type syenites in the northwest SSZ are likely related to oblique subduction Neo-Tethys and wrench tectonics trigger for the extensional pull-apart basin generations and magmatism. It is suggested that major strike-slip faults might also have played an important role during the emplacement of such intrusive rocks in the intra-arc extensional pull-apart basin. As a result, syenite rocks can be formed in different tectonic stages in a tectonic cycle.

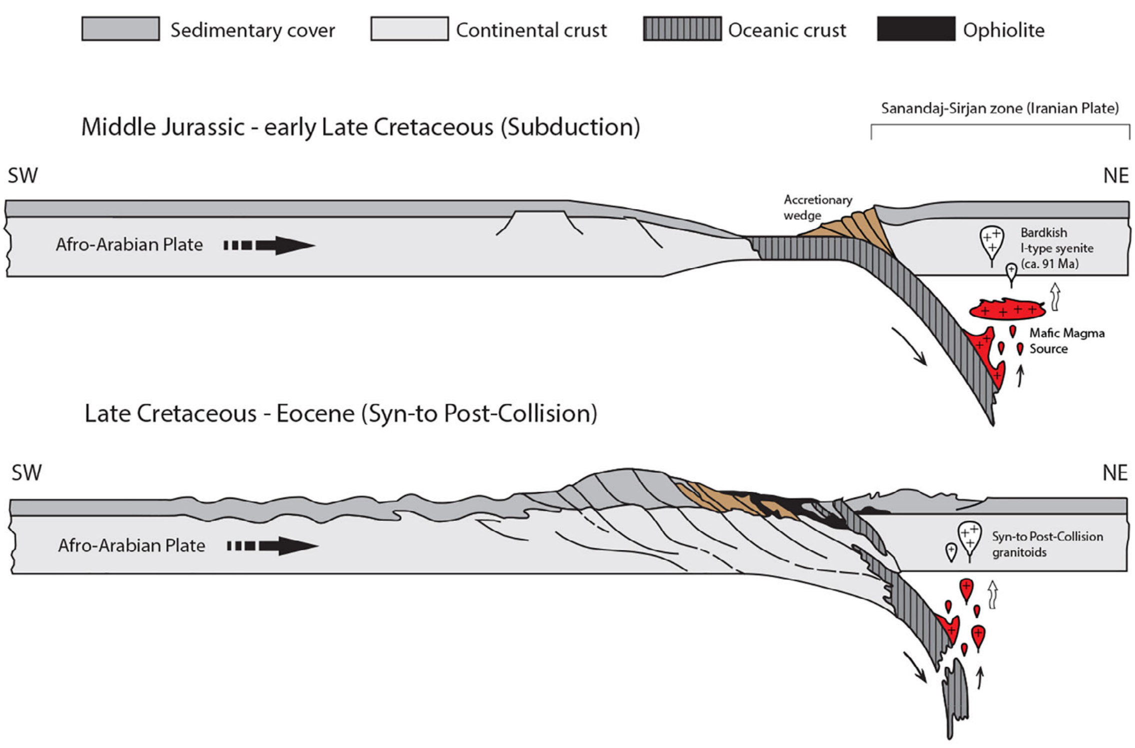

FIGURE 12 Schematic cross-sections, illustrating the evolution model for the Zagros orogenic belt in northwest Iran

TABLE 6 Isotope geochronological data from major plutonic rocks in the northwest SSZ

Pluton	Suite	Method	Age (Ma)	Error	Period	Tectonic setting	References
Marivan	Q-diorite	U–Pb	37.5	±8.0	Eocene	Post-collisional	Sepahi, Shahbazi, Siebel, and Ahmad (2014)
Nagadeh	Granite	U–Pb	41.8	±0.81	Eocene	—	Mazhari et al. (2011)
Piranshahr	Gabbro	U–Pb	40.7	±0.2	Eocene	Post-collisional	Mazhari et al. (2009)
	Gabbro	U–Pb	40.1	±0.8	Eocene	Post-collisional	
	Granite	U–Pb	41.3	±1.2	Eocene	Post-collisional	
	Granite	U–Pb	40.2	±1.4	Eocene	Post-collisional	
	Pulaskite	U–Pb	41.3	±0.8	Eocene	Post-collisional	
	Pulaskite	U–Pb	40.6	±1.6	Eocene	Post-collisional	
Baneh	Granite	U–Pb	36.69	±0.88	Eocene	Syn-collisional	Azizi, Hadad, Stern, and Asahara (2019)
	Granite	U–Pb	40.5	±0.56	Eocene	Syn-collisional	
	Granite	U–Pb	41	±0.98	Eocene	Syn-collisional	
Soursat	Granite	U–Pb	54.6	±1.6	Eocene	Syn- to post-collisional	Jamshidi-Badr, Collins, Masoudi, Cox, and Mohajjel (2013)
	Granite	U–Pb	56.2	±2.1	Eocene	Syn- to post-collisional	
	Syenogranite	U–Pb	59	±2.7	Paleocene	Early- to syn-collisional	
Hasan Salary	Granite	U–Pb	59.78	±0.1	Paleocene	—	Mahmoudi, Corfu, Masoudi, Mehrabi, and Mohajjel (2011)
Alvand	Q-diorite	K–Ar	73.8	±3.1	Late-Cretaceous	—	Baharifar, Bellon, Pique, and Moeinvaziri (2004)
	Pegmatite	K–Ar	74.7	±1.8	Late-Cretaceous	—	
	Granite	K–Ar	81.8	±1.9	Late-Cretaceous	—	
Urumieh	Granite	K–Ar	76	±3.4	Late-Cretaceous	Early collision	Ghalamghash et al. (2009)
	Granite	K–Ar	82	1.9	Late-Cretaceous	Early collision	
	Diorite	K–Ar	94.1	±2.3	Late-Cretaceous	Subduction-related	
	Diorite	K–Ar	94.8	±2.2	Late-Cretaceous	Subduction-related	
	Granite	K–Ar	98.9	±1.5	Late-Cretaceous	Subduction-related	
	Granite	K-Ar	100	±2.4	Late-Cretaceous	Subduction-related	
Hasan Salary	Granite	U–Pb	108.8	±0.3	Early-Cretaceous	Subduction-related	Mahmoudi et al. (2011)
Alvand	Diorite	K–Ar	135.2	±3.1	Early-Cretaceous	—	Baharifar et al. (2004)
Almogholagh	Diorite	Rb–Sr	144	±17	Early-Cretaceous	—	Valizadeh and Cantagrel (1975)
Suffi-abad	Granite	U–Pb	143.5	±2.3	Early-Cretaceous	Subduction related	Azizi, Tanaka, Asahara, Mehrabi, and Chung (2011)
	Felsic dike	U–Pb	147.5	±1.3	Late-Jurassic	Subduction related	
	Syenodiorite	U–Pb	147.5	±1.3	Late-Jurassic	Subduction related	
Gorveh	Gabbro	U–Pb	149.3	±0.2	Late-Jurassic	Subduction related	Mahmoudi et al. (2011)
	Monzonite	U–Pb	151	±0.2	Late-Jurassic	Subduction related	
	Granite	U–Pb	156.5	±0.6	Late-Jurassic	Subduction related	
Alvand	Granodiorite	U–Pb	154.4	±1.3	Late-Jurassic	Subduction-related	Shahbazi et al. (2010)
	Granite	U–Pb	161.7	±0.7	Late-Jurassic	Subduction-related	
	Granite	U–Pb	163.2	±1.1	Late-Jurassic	Subduction-related	
	Granite	U–Pb	163.9	±0.9	Late-Jurassic	Subduction-related	
	Diorite	U–Pb	165	±0.4	Middle-Jurassic	Subduction related	Mahmoudi et al. (2011)
	Granite	U–Pb	165.2	±0.2	Middle-Jurassic	Subduction related	
	Gabbro	U–Pb	166.5	±1.8	Middle-Jurassic	Subduction-related	Shahbazi et al. (2010)

7 | CONCLUSIONS

Zircon U–Pb dating has yielded precise crystallization ages of 91.3 ±1.1 Ma and 90.7 ±1.3 Ma for two samples of the Bardkish syenite, the weighted mean of 91.1 ±0.8 Ma, is the best estimate for the age of intrusion. Whole-rock chemical analyses are consistent with formation of the syenite magma in an arc system by fractional crystallization of a mafic parental magma with some crustal input. The parent magma was generated through partial melting of a lithospheric mantle source which had been enriched by metasomatism through subduction of the Neo-Tethys oceanic slab during the Turonian. The hornblende-plagioclase geothermometer and Al-in-hornblende geobarometer show that the Bardkish syenite crystallized at temperatures of 700–730 °C and depths of less than 11 km.

ACKNOWLEDGMENTS

Most of the laboratory work was carried out at the Research School of Earth Sciences, Australian National University. The authors thank Trevor Ireland for providing access to the SHRIMP facility, Vickie C. Bennett for her support with whole rock analyses and Shane Paxton for his contributions and assistance with zircon separation. We also appreciate Tatsuki Tsujimori and Yoshihiko Tamura for editorial efforts and invaluable comments and suggestions by anonymous referees.

ORCID

Amin Jafari https://orcid.org/0000-0002-4125-0087
Mohsen Moayyed https://orcid.org/0000-0002-7600-7482
Ian S. Williams https://orcid.org/0000-0003-4465-6493

REFERENCES

Adetunji, A., Olarewaju, V. O., Ocan, O. O., Macheva, L., & Ganevc, V. Y. (2018). Geochemistry and U–Pb zircon geochronology of Iwo quartz potassic syenite, southwestern Nigeria: Constraints on petrogenesis, timing of deformation and terrane amalgamation. *Precambrian Research*, *307*, 125–136.

Ahadnejad, V., Valizadeh, M. V., Deevsalar, R., & Rezaei-Kahkhaei, M. (2011). Age and geotectonic position of the Malayer granitoids: Implication for plutonism in the Sanandaj–Sirjan Zone, W Iran. *Neues Jahrbuch für Geologie und Paläontologie Abhandlungen*, *261*, 61–75.

Ajirlu, M. S., Moazzen, M., & Hajialioghli, R. (2016). Tectonic evolution of the Zagros Orogen in the realm of the Neotethys between the Central Iran and Arabian Plates: An ophiolite perspective. *Central European Geology*, *59*(1–4), 1–27.

Alavi, M. (1994). Tectonics of the Zagros orogenic belt of Iran: New data and interpretation. *Tectonophysics*, *229*, 211–238.

Allahyari, K., Saccani, E., Pourmoafi, M., Beccaluva, L., & Masoudi, F. (2010). Petrology of mantle peridotites and intrusive mafic rocks from the Kermanshah ophiolitic complex (Zagros belt, Iran): Implications for the geodynamic evolution of the Neo-Tethyan oceanic branch between Arabia and Iran. *Ofioliti*, *35*, 71–90.

Allen, C. M., & Chappell, B. W. (1992). Association of I-type granites with rift-related alkaline magmatism in Central Coastal Queensland, Australia. *Geological Society of America, Abstract Progress*, *24*(7), 43.

Amiri, M., Ahmad Khalaji, A., Tahmasbi, Z., Santos, S. J., Zarei Sahamieh, R., & Zamanian, H. (2017). Geochemistry, perrogenesis, and tectonic setting of the Almogholagh batholith in the SanandajeSirjan zone, western Iran. *Journal of African Earth Sciences*, *134*, 113–133.

Anderson, J. L., Barth, A. P., Wooden, J. L., & Mazdab, F. (2008). Thermometers and thermobarometers in granitic systems. In K. Putirka, & F. Tepley (Eds.), Minerals, inclusions and volcanic processes. *Reviews in Mineralogy and Geochemistry*, *69*, 121–142.

Anderson, J. L., & Smith, D. R. (1995). The effects of temperature and fO_2 on the Al-in-hornblende barometer. *American Mineralogist*, *8*, 549–559.

Angiolini, L., Balini, M., Garzanti, E., Nicora, A., & Tintori, A. (2003). Gondwanan deglaciation and opening of Neotethys: The Al Khlata and Saiwan Formations of Interior Oman. *Palaeogeography, Palaeoclimatology, Palaeoecology*, *196*, 99–123.

Arefifard, S. (2017). Foraminiferal-based paleobiogeographic reconstructions in the Carboniferous of Iran and its implications for the Neo-Tethys opening time: A synthesis. *Geologica Acta*, *15*, 135–151.

Armon, S. (2017). *Geochronology and petrology of intrusive rocks in Bardkish and Balestan, NW Iran* (MSc thesis). Damghan University.

Arvin, M., Pan, Y., Dargahi, S., Malekizadeh, A., & Babaei, A. (2007). Petrochemistry of the Siah-Kuh granitoid stock southwest of Kerman Iran: Implications for initiation of Neotethys subduction. *Journal of Asian Earth Sciences*, *30*, 474–489.

Azizi, H., Hadad, S., Stern, R. J., & Asahara, Y. (2019). Age, geochemistry, and emplacement of the∼40-Ma Baneh granite–appinite complex in a transpressional tectonic regime, Zagros suture zone, northwest Iran. *International Geology Review*, *61*(2), 195–223.

Azizi, H., Tanaka, T., Asahara, Y., Mehrabi, B., & Chung, S. L. (2011). Geochronological and geochemical constraints on the petrogenesis of high-K granite from the Suffiabad area, Sanandaj-Sirjan zone, NW Iran. *Chemie der Erde*, *71*, 363–376.

Baharifar, A. A., Bellon, H., Pique, A., & Moeinvaziri, H. (2004). The crystalline complexes of Hamadan (Sanandaj-Sirjan zone, western Iran): Metasedimentary Mesozoic sequences affected by late cretaceous tectono-metamorphic and plutonic events. *Comptes Rendus Geoscience*, *336*, 1443–1452.

Berberian, M., & King, G. C. P. (1981). Towards a paleogeography and tectonic evolution of Iran. *Canadian Journal of Earth Sciences*, *18*, 210–265.

Berger, A., Burri, T., Alt-Epping, P., & Engi, M. (2008). Tectonically controlled fluid flow and water-assisted melting in the middle crust: An example from the Central Alps. *Lithos*, *102*, 598–615.

Black, L. P., Kamo, S. L., Allen, C. M., Davis, D. W., Aleinikoff, J. N., Valley, J. W., … Foudoulis, C. (2004). Improved $^{206}Pb/^{238}U$ microprobe geochronology by the monitoring of a trace-element-related matrix effect: SHRIMP, ID-TIMS, ELA-ICP-MS and oxygen isotope documentation for a series of zircon standards. *Chemical Geology*, *205*, 115–140.

Bonin, B. (2007). A-type granites and related rocks: Evolution of a concept, problems and prospects. *Lithos*, *97*, 1–29.

Bora, S., Kumar, S., Yi, K., Kim, N., & Lee, T. H. (2013). Geochemistry and U–Pb SHRIMP zircon chronology of granitoids and microgranular enclaves from Jhirgadandi Pluton of Mahakoshal belt, Central India tectonic zone India. *Journal of Asian Earth Sciences*, *70–71*, 99–114.

Brown, P. E., & Becker, S. M. (1986). Fractionation, hybridisation and magma-mixing in the Kialineq centre East Greenland. *Contributions to Mineralogy and Petrology*, *92*, 57–70.

Burmakina, G. N., & Tsygankov, A. A. (2013). Mafic microgranular enclaves in Late Paleozoic granitoids in the Burgasy quartz syenite massif, Western Transbaikalia: Composition and petrogenesis. *Petrology*, *21*, 280–303.

Chen, B., Chen, Z. C., & Jahn, B. M. (2009). Origin of mafic enclaves from the Taihang Mesozoic orogen, north China craton. *Lithos*, *110*, 343–358.

Chen, J. F., Xie, Z., Li, H. M., Zhang, X. D., Zhou, T. X., Park, Y. S., … Zhang, X. (2003). U-Pb zircon ages for a collision-related K-rich complex at Shidao in the Sulu ultrahigh pressure terrane, China. *Geochemical Journal*, *37*, 35–46.

Chiu, H. Y., Chung, S. L., Zarrinkoub, M. H., Mohammadi, S. S., Khatib, M. M., & Iizuka, Y. (2013). Zircon U–Pb age constraints from Iran on the magmatic evolution related to Neotethyan subduction and Zagros orogeny. *Lithos*, *162–163*, 70–87.

Cumming, G. L., & Richards, J. R. (1975). Ore lead isotope ratios in a continuously changing earth. *Earth and Planetary Science Letters*, *28*, 155–171.

Davoudian, A., Hamedani, A., Shabanian, N., & Mackizadeh, M. A. (2007). Petrological and geochemical constraints on the evolution of the

Cheshmeh-Sefid granitoid complex of Golpaygan in the Sanandaj-Sirjan zone, Iran. *Neues Jahrbuch für Mineralogie Abhandlungen*, *184*(2), 117–129.

Deer, W. A., Howie, R. A., & Zussman, J. (1992). *An introduction to the rock-forming minerals* (2nd ed.). Harlow: Prentice Hall.

Eyal, M., Litvinovsky, B., Jahn, B. M., Zanvilevich, A., & Katzir, Y. (2010). Origin and evolution of post-collisional magmatism: Coeval Neoproterozoic calc-alkaline and alkaline suites of the Sinai Peninsula. *Chemical Geology*, *269*, 153–179.

Fazlnia, A. (2018). Petrogenesis and tectonic significance of Sardasht syenite–monzonite–gabbro–appinite intrusions, NW Iran. *International Journal of Earth Sciences*, *108*, 49–66.

Ferreira, V. P., Sial, A. N., Pimentel, M. M., Armstrong, R., Guimarães, I. P., da Silva Filho, A. F., … da Silva, T. R. (2015). Reworked old crust-derived shoshonitic magma: The Guarany pluton, Northeastern Brazil. *Lithos*, *232*, 150–161.

Gervasoni, F., Klemme, S., Rocha-Júnior, E., & Berndt, J. (2016). Zircon saturation in silicate melts: A new and improved model for aluminous and alkaline melts. *Contributions to Mineralogy and Petrology*, *171*(3), 21. https://doi.org/10.1007/s00410-016-1227-y

Ghalamghash, J., Bouchez, J. L., Vosoughi-Abedini, M., & Nedelec, A. (2009). The Urumieh plutonic complex (NW Iran): record of the geodynamic evolution of the Sanandaj-Sirjan zone during cretaceous times - Part I: petrogenesis and K/Ar dating. *Journal of Asian Earth Sciences*, *35*, 401-415.

Ghazi, A. M., Pessagno, E. A., Hassanipak, A. A., Duncan, R. A., & Babaie, H. A. (2003). Biostratigraphic zonation and $^{40}Ar–^{39}Ar$ ages for the neotethyan Khoy ophiolite of NW Iran. *Palaeogeography*, *Palaeoclimatology*, *Palaeoecology*, *193*, 311–323.

Hajialioghli, R., & Moazzen, M. (2014). Supra-subduction and mid-ocean ridge peridotites from the Piranshahr area, NW Iran. *Journal of Geodynamics*, *81*, 41–55.

Hammarstrom, J. M., & Zen, E. (1986). Aluminum in hornblende: An empirical igneous geobarometer. *American Mineralogist*, *71*, 1297–1313.

Hassanzadeh, J., & Wernicke, B. P. (2016). The Neotethyan Sanandaj-Sirjan zone of Iran as an archetype for passive margin-arc transitions. *Tectonics*, *35*, 586–621.

Hempton, M. R. (1987). Constraints on Arabian plate motion and extensional history of the Red Sea. *Tectonics*, *6*, 687–705.

Holland, T., & Blundy, J. (1994). Non-ideal interactions in calcic amphiboles and their bearing on amphibole-plagioclase thermometer. *Contributions to Mineralogy and Petrology*, *116*, 433–447.

Hollister, L. S., Grisson, G. C., Peters, E. K., Stowell, H. H., & Sisson, V. B. (1987). Confirmation of the empirical correlation of Al in hornblende with pressure of solidification of calc-alkaline plutons. *American Mineralogist*, *72*, 231–239.

Huang, W. L., & Wyllie, P. J. (1981). Phase relationship of S-type granite with H_2O to 35 kbar: Muscovite granite from Harney Peak, South Dakota. *Journal of Geophysical Research*, *86*, 10515–10529.

Jafari, A., Fazlnia, A. N., & Jamei, S. (2018). Geochemistry, petrology and geodynamic setting of the Urumieh plutonic complex, Sanandaj-Sirjan zone, NW Iran: New implication for Arabian and Central Iranian plate collision. *Journal of African Earth Sciences*, *139*, 421–439.

Jahn, B. M., Litvinovsky, B. A., Zanvilevich, A. N., & Reichow, M. (2009). Peralkaline granitoid magmatism in the Mongolian-Transbaikalian Belt: Evolution, petrogenesis and tectonic significance. *Lithos*, *113*, 521–539.

James, G. A., & Wynd, J. G. (1965). Stratigraphic nomenclatures of Iranian oil consortium agreement area. *AAPG Bulletin*, *49*, 2182–2245.

Jamshidi-Badr, M., Collins, A. S., Masoudi, F., Cox, G., & Mohajjel, M. (2013). The U–Pb age, geochemistry and tectonic significance of granitoids in the Soursat Complex, Northwest Iran. *Turkish Journal of Earth Sciences*, *22*, 1–31.

Jamshidi-Badr, M., Collins, A. S., Salomao, G. N., & Costa, M. (2018). U–Pb zircon ages, geochemistry and tectonic setting of felsic and mafic intrusive rocks of Almogholagh complex, NW Iran. *Periodico di Mineralogia*, *87*, 21–53.

Jiang, Y. H., Jiang, S. Y., Ling, H. F., Zhou, X. R., Rui, X. J., & Yang, W. Z. (2002). Petrology and geochemistry of shoshonitic plutons from the western Kunlun orogenic belt, northwestern Xinjiang, China: Implications for granitoid geneses. *Lithos*, *63*, 165–187.

Johnson, M. C., & Rutherford, M. J. (1989). Experimental calibration of the aluminum-in-hornblende geobarometer with application to Long Valley caldera (California) volcanic rocks. *Geology*, *17*, 837–841.

Kaul, P. F. T., & Cordiani, U. G. (2000). Geochemistry of Serra do Mar granitic magmatism and tectonic implications, southern Brazil. *Revista Brasileira de Geo iencias*, *30*(1), 115–119.

Khalatbari Jafari, M., Juteau, T., & Cotton, J. (2006). Petrological and geochemical study of the Late Cretaceous ophiolite of Khoy (NW Iran), and related geological formations. *Journal of Asian Earth Sciences*, *27*, 465–502.

Kumar, S., Pieru, T., Rino, V., & Hayasaka, Y. (2017). Geochemistry and U–Pb SHRIMP zircon geochronology of microgranular enclaves and host granitoids from South Khasi Hills of the Meghalaya Plateau, NE India: Evidence of synchronous mafic–felsic magma mixing–fractionation and diffusion in a post-collision tectonic environment during the Pan-African orogenic cycle. *Geological Society*, *London*, *Special Publications*, *457*, 253–289.

Le Bas, M. J., Le Maitre, R. W., Streckeisen, A., & Zanettin, B. (1986). A chemical classification of volcanic rocks on the total alkali-silica diagram. *Journal of Petrology*, *27*, 745–750.

Leake, B. E., Woolley, A. R., Arps, C. E., Birch, W. D., Gilbert, M. C., Grice, J. D., … Youzhi, G. (1997). Nomenclature of amphiboles: Report of the subcommittee on amphiboles of the international mineralogical association commission on new minerals and mineral names. *The Canadian Mineralogist*, *35*, 219–246.

Litvinovsky, A. A., Jahn, B. M., Zanvilevich, A. N., Saunders, A., Poulain, S., Kuzmin, D. V., … Titov, A. V. (2002). Petrogenesis of syenite–granite suites from the Bryansky Complex (Transbaikalia, Russia): Implications for the origin of A-type granitois magmas. *Chemical Geology*, *189*, 105–133.

Litvinovsky, B. A., Jahn, B. M., & Eyal, M. (2015). Mantle-derived sources of syenites from the A-type igneous suites – New approach to the provenance of alkaline silicic magmas. *Lithos*, *232*, 242–265.

Lubala, R. T., Frick, C., Roders, J. H., & Walraven, F. (1994). Petrogenesis of syenites and granites of the Schiel Alkaline Complex, Northern Transvaal, Southern Africa. *Journal of Geology*, *102*, 307–309.

Ludwig, K. R. (2003). *Isoplot 3*. Berkeley, CA: Berkeley Geochronology Center, Special publication, 4.

Lynch, D. J., Musselman, T. E., Gutmann, J. T., & Patchett, P. J. (1993). Isotopic evidence for the origin of Cenozoic volcanic rocks in the Pinacate volcanic field, northwestern Mexico. *Lithos*, *29*, 295–302.

Mahmoudi, S., Corfu, F., Masoudi, F., Mehrabi, B., & Mohajjel, M. (2011). U–Pb dating and emplacement history of granitoid plutons in the Northern Sanandaj-Sirjan zone, Iran. *Journal of Asian Earth Sciences*, *41*, 238–249.

Maniar, P. D., & Piccoli, P. M. (1989). Tectonic discrimination of granitoids. *Geological Society of America Bulletin*, *101*, 635–643.

Martin, R. F., & Devito, C. (2005). The patterns of enrichment in felsic pegmatites ultimately depend on tectonic setting. *Canadian Mineralogist*, *43*, 2027–2048.

Masoudi, F., Yardley, B. W. D., & Cliff, R. A. (2002). Rb–Sr geochronology of pegmatites, plutonic rocks and a hornfels in the region southwest of Arak, Iran. *Journal of Sciences*, *13*(3), 249–254.

Mazhari, S. A., Amini, S., Ghalamghash, J., & Bea, F. (2011). Petrogenesis of granitic unit of Naqadeh complex, Sanandaj–Sirjan Zone, NW Iran. *Arabian Journal of Geosciences*, *4*, 59–67.

Mazhari, S. A., Bea, F., Amini, S., Ghalamghash, J., Molina, J. F., Montero, P., … Williams, I. S. (2009). The Eocene bimodal Piranshahr massif of the Sanandaj–Sirjan Zone, NW Iran: A marker of the end of the collision in the Zagros orogen. *Journal of the Geological Society*, *166*, 53–69.

McCall, G. J. H. (2002). A summary of the geology of the Iranian Makran. *Geological Society of London Special Publication*, *195*, 147–204.

McDonough, W. F., & Sun, S. S. (1995). The composition of the earth. *Chemical Geology*, *120*, 223–253.

Mingram, B., Trumbull, R. B., Littman, S., & Gerstenberger, H. (2000). A petrogenetic study of androgenic felsic magmatism in the Cretaceous Paresis ring complex, Namibia: Evidence for mixing of crust and mantle-derived components. *Lithos*, *54*, 1–22.

Mohajjel, M., Fergusson, C. L., & Sahandi, M. R. (2003). Cretaceous–Tertiary convergence and continental collision Sanandaj-Sirjan zone western Iran. *Journal of Asian Earth Sciences*, *21*, 397–412.

Mohammadi, E., Rezapour, M., Sodoudi, F., & Sadidkhouy, A. (2014). New seismic imaging of some tectonic zones in the Iranian Plateau. *Journal of the Earth and Space Physics*, *40*, 1–12.

Morrison, G. W. (1980). Characteristics and tectonic setting of the shoshonite rock association. *Lithos*, *13*, 97–108.

Mushkin, A., Navon, O., Halicz, L., Hartmann, G., & Stein, M. (2003). The petrogenesis of A-type magmas from the Amram Massif, Southern Israel. *Journal of Petrology*, *44*, 815–832.

Nabavi, M. H. (1976). An introduction to geology of Iran. *Geological Survey of Iran Publication*, 110 pp.

Naghizadeh, R., & Ghalamghash, J. (2005). Geological map of Oshnavieh 1: 100,000, *Geological Survey of Iran*.

Pearce, J. A. (1983). Role of the sub-continental lithosphere in magma genesis at active continental margins. In C. J. Hawkesworth & M. J. Norry (Eds.), *Continental basalts and mantle xenoliths* (pp. 230–249). Nantwich: Shiva Publications.

Rapp, R. P., & Watson, E. B. (1995). Dehydration melting of meta-basalt at 8–32 kbar: Implications for continental growth and crust–mantle recycling. *Journal of Petrology*, *36*, 891–931.

Rezaei Bargoshadi, M., Moazzen, M., & Yang, T. N. (2019). Geochemistry of arc-related mantle peridotites and gabbros from the Chaldoran ophiolite, NW Iran. *International Geology Review*, *62*, 1724–1750. https://doi.org/10.1080/00206814.2019.1663767

Rezaii, L., & Moazzen, M. (2014). Mineral chemistry of the ophiolitic peridotites and gabbros from the Serow area: Implications for tectonic setting and locating the Neotethys suture in NW Iran. *Central European Geology*, *57*, 385–402.

Riishuus, M. S., Peate, D. W., Tegner, C., Wilson, J. R., Brooks, C. K., & Waight, T. E. (2005). Petrogenesis of syenites at a rifted continental margin: Origin, contamination and interaction of alkaline mafic and felsic magmas in the Astrophyllite Bay Complex, East Greenland. *Contributions to Mineralogy and Petrology*, *149*, 350–371.

Robertson, A. H. F., Parlak, O., Rízaoğlu, T., Ünlügenç, Ü., İnan, N., Tasli, K., & Ustaömer, T. (2007). Tectonic evolution of the South Tethyan Ocean: Evidence from the Eastern Taurus Mountains (Elaziğ region, SE Turkey). *The Geological Society of London*, *272*, 231–270.

Sarjoughian, F., Kananian, A., Haschke, M., & Ahmadian, J. (2015). Transition from I-type to A-type magmatism in the Sanandaj–Sirjan Zone, NW Iran: An extensional intra-continental arc. *Geological Journal*, *51* (3), 387–404.

Schiano, P., Monzier, M., Eissen, J. P., Martin, H., & Koga, K. T. (2010). Simple mixing as the major control of the evolution of volcanic suites in the Ecuadorian Andes. *Contributions to Mineralogy and Petrology*, *160* (2), 297–312.

Schmidt, M. W. (1992). Amphibole composition in tonalite as a function pressure: An experimental calibration of the Al-in-hornblende barometer. *Contributions to Mineralogy and Petrology*, *110*, 304–310.

Sepahi, A. A., & Athari, S. F. (2006). Petrology of major granitic plutons of the northwestern part of the Sanandaj-Sirjan Metamorphic Belt, Zagros Orogen, Iran: With emphasis on A-type granitoids from the SE Saqqez area. *Neues Jahrbuch für Mineralogie Abhandlungen*, *183*(1), 93–106.

Sepahi, A. A., Ghoreishvandi, H., Maanijou, M., Maruoka, T., & Vahidpour, H. (2020). Geochemical description and sulfur isotope data for Shahrak intrusive body and related Fe-mineralization (east Takab), northwest Iran. *Island Arc*, *29*, e12367.

Sepahi, A. A., Shahbazi, H., Siebel, W., & Ahmad, R. (2014). Geochronology of plutonic rocks from the Sanandaj-Sirjan zone, Iran and new zircon and titanite U–Th–Pb ages for granitoids from the Marivan pluton. *Geochronometria*, *41*, 207–215.

Sepehr, M., & Cosgrove, J. W. (2004). Structural framework of the Zagros Dold–Thrust Belt, Iran. *Marine and Petroleum Geology*, *21*, 829–843.

Shahbazi, H., Siebel, W., Pourmoafee, M., Ghorbani, M., Sepahi, A. A., Shang, C. K., & Vousoughi-Abedini, M. (2010). Geochemistry and UePb zircon geochronology of the Alvand plutonic complex in Sanandaj Sirjan zone (Iran): New evidence for Jurassic magmatism. *Journal of Asian Earth Sciences*, *39*, 668–683.

Shellnutt, J. G., Zhou, M. F., & Zellmer, G. F. (2009). The role of Fe–Ti oxide crystallization in the formation of A-type granitoids with implications for the Daly gap: An example from the Permian Baima igneous complex, SW China. *Chemical Geology*, *259*, 204–217.

Sherkati, S., Letouzey, J., & Frizon de Lamotte, D. (2006). Central Zagros fold-thrust belt (Iran): New insights from seismic data, field observation, and sandbox modeling. *Tectonics*, *25*, TC4007. https://doi.org/10.1029/2004TC001766

Slagstad, T., Jamieson, R. A., & Culshaw, N. G. (2005). Formation, crystallization, and migration of melt in the midorogenic crust: Muskoka domain migmatites, Grenville Province, Ontario. *Journal of Petrology*, *46*, 893–919.

Stampfli, G. M. (2000). Tethyan oceans. *GSL Special Publications*, *173*, 1–23.

Stöcklin, J. (1968). Structural history and tectonics of Iran: A review. *AAPG Bulletin*, *52*, 1229–1258.

Sun, S. S., & McDonough, W. F. (1989). Chemical and isotopic systematic of oceanic basalts: Implications for mantle composition and processes. In A. D. Saunders & M. J. Norry (Eds.), *Magmatism in the ocean basins* GSL Special Publications (Vol. 42, pp. 313–345).

Sutcliffe, R. H., Smith, A. R., Doherty, W., & Barnett, R. L. (1990). Mantle derivation of Archean amphibole-bearing granitoids and associated mafic rocks: Evidence from the southern Superior Province, Canada. *Contributions to Mineralogy and Petrology*, *105*, 255–274.

Swain, G., Barovich, K., Hand, M., Ferris, G., & Schwarz, M. (2008). Petrogenesis of the St Peter Suite, southern Australia: Arc magmatism and Proterozoic crustal growth of the South Australian Craton. *Precambrian Research*, *166*, 283–296.

Tchameni, R., Mezger, K., Nsifa, N. E., & Pouclet, A. (2001). Crustal origin of early Proterozoic syenites in the Congo Craton (Ntem Complex), South Cameroon. *Lithos*, *57*, 23–42.

Thorpe, R. S., & Tindle, A. G. (1992). Petrology and petrogenesis of a Tertiary bimodal dolerite-peralkaline/subalkaline-trachyte/rhyolite dyke association from Lundy, Bristol Channel, UK. *Geological Journal*, *27*, 101–117.

Tulloch, A. J., & Challis, G. A. (2000). Emplacement depths of Paleozoic–Mesozoic plutons from western New Zealand estimated by hornblende-Al geobarometry. *New Zealand Journal of Geology and Geophysics*, *43*, 555–567.

Turner, S., Arnaud, N., Liu, J., Rogers, N., Hawkesworth, C., Harris, N., … Deng, W. (1996). Post-collision, Shoshonitic volcanism on the Tibetan Plateau: Implications for convective thinning of the lithosphere and the source of ocean Island basalts. *Journal of Petrology*, *37*(1), 45–71.

Valizadeh, M. V., & Cantagrel, J. M. (1975). Premieres donnees radiometriques (K–Ar et Rb–Sr) sur les micas du complexe magmatique du Mont Alvand pres Hamedan (Iran Occidental). *Comptes rendus hebdomadaires des séances de l'Académie des sciences, Série D, Sciences naturelles*, *281*, 1083–1086.

Vernikovsky, V. A., Pease, V. L., Vernikovskaya, A. E., Romanov, A. P., Gee, D. G., & Travin, V. A. (2003). First report of early Triassic A-type granite and syenite intrusions from Taimyr: Product of the northern Eurasian superplume. *Lithos*, *66*, 23–66.

Wang, K., Liu, S., Wang, M., & Yan, M. (2017). Geochemistry and zircon U–Pb–Hf isotopes of the late Neoarchean granodiorite-monzogranite-quartz syenite intrusions in the Northern Liaoning Block, North China Craton: Petrogenesis and implications for geodynamic processes. *Precambrian Research*, *295*, 151–171.

Whalen, J. B., Currie, K. L., & Chappel, B. W. (1987). A-type granites: Geochemical characteristics, discrimination and petrogenesis. *Contributions to Mineralogy and Petrology*, *95*, 407–419.

Whitney, D. L., & Evans, B. W. (2010). Abbreviations for names of rock-forming minerals. *American Mineralogist*, *95*, 185–187.

Williams, I. S. (1998). Chapter 1, U–Th–Pb geochronology by ion microprobe. In M. A. McKibben, W. C. Shanks III, & W. I. Ridley (Eds.), Applications of microanalytical techniques to understanding mineralizing processes. *Reviews of Economic Geology*, *7*, 1–35.

Woodhead, J. D., Hergt, J. M., Davidson, J. P., & Eggins, S. M. (2001). Hafnium isotope evidence for 'conservative' element mobility during subduction zone processes. *Earth and Planetary Science Letters*, *192*, 331–346.

Wu, C. Z., Zhang, Z. Z., Gu, L. X., Tang, J. H., & Lei, R. X. (2010). Sr, Nd and O isotopic characters of quartz syenites in the Weiya magmatic complex from eastern Tianshan in NW China: Melting of the thickened juvenile lower crust. *Geochemical Journal*, *44*, 285–298.

Wyllie, P. J., & Sekine, T. (1982). The formation of mantle phlogopite in subduction zone hybridization. *Contributions to Mineralogy and Petrology*, *79*, 375–380.

Yan, X., & Jiang, S. Y. (2019). Petrogenesis and tectonic implications of Early Cretaceous shoshonitic syenites in the northern Wuyi Mt Range, Southeast China. *Journal of Asian Earth Sciences*, *180*, 103877. https://doi.org/10.1016/j.jseaes.2019.103877

Yang, J. H., Chung, S. L., Wilde, S. A., Wu, F. Y., Chu, M. F., Lo, C. H., & Fan, H. R. (2005). Petrogenesis of post-orogenic syenites in the Sulu Orogenic Belt, East China: Geochronological, geochemical and Nd–Sr isotopic evidence. *Chemical Geology*, *214*, 99–125.

Zanchi, A., Zanchetta, S., Berra, F., Mattei, M., Garzanti, E., Molyneux, S., … Sabouri, J. (2009). The Eo-Cimmerian (Late? Triassic) orogeny in North Iran. *GSL Special Publications*, *312*, 31–56.

Zhu, J., Wang, L., Peng, S., Peng, L., Wu, C., & Qiu, X. (2017). U–Pb zircon age, geochemical and isotopic characteristics of the Miaoya syenite and carbonatite complex, Central China. *Geological Journal*, *52*, 938–954.

Zhu, X., Chen, F., Nie, H., Siebel, W., Yang, Y., Xue, Y., & Zhai, M. (2014). Neoproterozoic tectonic evolution of south Qinling, China: Evidence from zircon ages and geochemistry of the Yaolinghe volcanic rocks. *Precambrian Research*, *245*, 115–130.

SUPPORTING INFORMATION

Additional supporting information may be found online in the Supporting Information section at the end of this article.

How to cite this article: Jafari A, Moayyed M, Williams IS. The age and geochemistry of the Bardkish syenite, northwest Iran: Syenite formation during Neo-Tethyan subduction. *Island Arc*. 2020;29:e12375. https://doi.org/10.1111/iar.12375